CMS Physics Analysis Summary

Contact: cms-pag-conveners-higgs@cern.ch 2018/03/14

Search for invisible decays of the Higgs boson produced through vector boson fusion at $\sqrt{s} = 13$ TeV

The CMS Collaboration

Abstract

A search for invisible decays of the Higgs boson is performed using 13 TeV proton-proton collision data collected by the CMS experiment at the LHC in 2016, corresponding to an integrated luminosity of 35.9 fb^{-1}. The search targets the production of the Higgs boson through vector boson fusion. The data are found to be in agreement with the predicted background contributions from standard model processes. An observed (expected) upper limit of 0.28 (0.21), at 95% confidence level, is placed on the invisible branching fraction of the 125 GeV Higgs boson. Upper limits are also computed on the product of the cross section and branching fraction of a scalar Higgs boson-like particle, with mass ranging between 110 and 1000 GeV. Finally, a combination of several analyses searching for invisible decays of the Higgs boson, based on 35.9 fb^{-1} of data collected by the CMS detector in 2016, is performed. An observed (expected) upper limit of 0.24 (0.18) is placed on the invisible branching fraction. This result is also interpreted in the context of Higgs-portal dark matter models, setting upper bounds on the spin-independent dark matter-nucleon scattering cross section.

1 Introduction

Since the discovery of the Higgs boson at the CERN LHC [1–3], the ATLAS and CMS Collaborations have pursued a wide-ranging program to study its properties and interactions. Precise measurements of the Higgs boson couplings to standard model (SM) particles have set an indirect upper limit, at 95% confidence level (CL), of 34% on the Higgs boson branching fraction to non-SM particles [4]. In the SM, the Higgs boson decays invisibly only through the $\mathrm{H} \to \mathrm{ZZ} \to 4\nu$ process, with a branching fraction, $\mathcal{B}(\mathrm{H} \to \mathrm{inv})$, of about 0.1%. While such a small rate of invisible decays cannot be currently probed at the LHC, $\mathcal{B}(\mathrm{H} \to \mathrm{inv})$ may be significantly enhanced in the context of physics scenarios beyond the SM [5–7]. Previous searches performed by the ATLAS and CMS Collaborations have set upper limits at 95% CL of 0.25 [8] and 0.24 [9] on $\mathcal{B}(\mathrm{H} \to \mathrm{inv})$, respectively.

This letter presents a search for invisible decays of the Higgs boson, performed using 13 TeV proton-proton (pp) collision data collected by the CMS detector at the LHC, corresponding to an integrated luminosity of $35.9\,\mathrm{fb}^{-1}$. The search targets events in which the Higgs boson is produced in association with jets from vector boson fusion (VBF, via $\mathrm{qq} \to \mathrm{qqH}$), as illustrated in Fig. 1 (left). In these events, the Higgs boson is produced in association with two jets that have a large pseudorapidity gap ($\Delta\eta_{\mathrm{jj}}$), and form a large dijet invariant mass (m_{jj}). This characteristic signature allows the suppression of SM backgrounds, making the qqH channel the most sensitive search for invisible decays of the Higgs boson at hadron colliders. The search is performed via two different approaches. In one case, referred to as the "cut-and-count analysis", the signal is extracted by performing a fit to the total number of events passing an optimized selection that exploits the differences in the kinematic properties between signal and background processes. In the second case, referred to as the "shape analysis", a fit is performed to the binned dijet mass distribution of events passing a more relaxed phase-space selection. The results obtained from the former approach can be directly translated into a limit on the visible cross section in a model-independent way, while the shape analysis has been designed to improve the sensitivity compared to the approach used in earlier CMS publications [9, 10]. The results are also interpreted as a search for an additional SM-like Higgs boson with an invariant mass between 110 to 1000 GeV, which does not mix with the 125 GeV Higgs.

Finally, a combination of searches for invisible decays of the Higgs boson, using data collected by the CMS detector during 2016, is presented. The searches target the qqH, the associated production (VH, where V denotes W or Z boson), and the gluon fusion (ggH) modes. The VH channels include both a search for ZH production, in which the Z boson decays leptonically ($\ell = \mu, e$) [11], and one for VH modes where the W or Z boson decays to high p_T jets [12]. Additional sensitivity is achieved by including a search for ggH production, where a high p_{T} Higgs boson candidate is produced in association with initial state radiated jets [12]. The Feynman diagrams for the qqH, VH, and ggH production processes are shown in Fig. 1. The result of the combination is further interpreted in the context of Higgs-portal models of dark matter (DM) interactions [13–17], in which the 125 GeV Higgs boson plays the role of a mediator between SM and DM particles, thereby allowing the possibility of producing DM at the LHC.

2 The CMS detector

The CMS detector is a multi-purpose apparatus designed to study a wide range of physics processes in both pp and heavy ion collisions. The central feature of the experiment is a superconducting solenoid of 6 m internal diameter, providing a magnetic field of 3.8 T parallel to the beam direction. Within the solenoid volume a silicon pixel and strip tracker, a lead tungstate

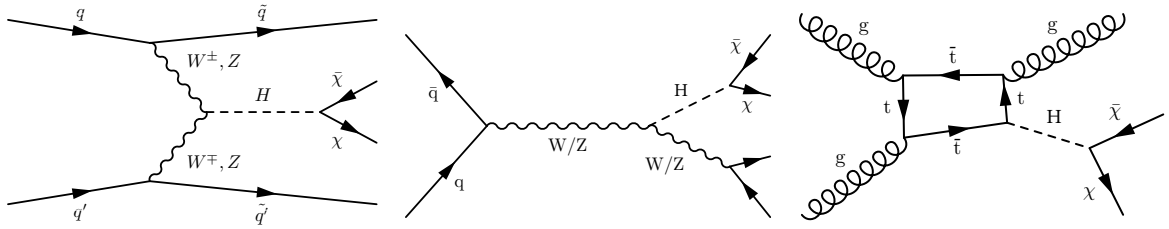

Figure 1: Feynman diagrams for the main production processes targeted in the searches considered in the combination: qq $\to$ qqH (left), qq $\to$ VH (center), and gg $\to$ gH (right).

crystal electromagnetic calorimeter (ECAL), and a brass and scintillator hadron calorimeter (HCAL) are installed, each composed of a barrel and two endcap sections. The tracker system measures the momentum of charged particles up to a pseudorapidity of $|\eta| = 2.5$, while the electromagnetic and the hadron calorimeters provide coverage up to $|\eta| = 3$. Moreover, the steel and quartz-fiber Čerenkov hadron forward calorimeter (HF) extends the coverage to $|\eta| = 5$. Muons are detected in gas-ionization chambers embedded in the steel flux-return yoke outside the solenoid, which cover up to $|\eta| = 2.4$.

Events of interest are selected using a two-tiered trigger system [18]. The first level (L1) is composed by custom hardware processors, which use information from the calorimeters and muon detectors to select events at a rate of about 100 kHz. The second level, known as high-level trigger (HLT), is a software based system which runs a version of the CMS full event reconstruction optimized for fast processing, reducing the event rate to about 1 kHz.

A more detailed description of the CMS detector, together with a definition of the coordinate system used and the relevant kinematic variables, can be found in Ref. [19].

3 Event reconstruction

The particle-flow (PF) event algorithm [20] reconstructs and identifies each individual particle with an optimized combination of information from the various elements of the CMS detector. The energy of photons is directly obtained from the ECAL measurement, corrected for zero-suppression effects. The energy of electrons is determined from a combination of the electron momentum at the primary interaction vertex, as determined by the tracker, the energy of the corresponding ECAL cluster, and the energy sum of all bremsstrahlung photons spatially compatible with originating from the electron track. The energy of muons is obtained from the curvature of the corresponding tracks. The energy of charged hadrons is determined from a combination of their momentum measured in the tracker and the matching of ECAL and HCAL energy deposits, corrected for zero-suppression effects and for the response function of the calorimeters to hadronic showers. Finally, the energy of neutral hadrons is obtained from the corresponding corrected ECAL and HCAL energy.

The missing transverse momentum vector ($\vec{p}_{\mathrm{T}}^{\,\mathrm{miss}}$) is computed as the negative vector sum of the transverse momenta (p_{T}) of all the PF candidates in an event, and its magnitude is denoted as $p_{\mathrm{T}}^{\mathrm{miss}}$. Hadronic jets are reconstructed by clustering PF candidates through the anti-k_{T} algorithm [21, 22], with a distance parameter of 0.4. The reconstructed vertex, with the largest value of summed physics-object p_{T}^2, is taken to be the primary pp interaction vertex. The charged PF candidates originating from any other vertex are ignored during the jet finding procedure. Jet momentum is determined as the vectorial sum of all particle momenta inside the jet, and is found, from simulation, to be within 5 to 10% of the true momentum over the whole p_{T} spectrum and detector acceptance. An offset correction is applied to jet energies to take into account

the contribution from additional pp interactions within the same or adjacent bunch crossings (pileup). Jet energy corrections are derived from simulation and are confirmed with *in situ* measurements of the energy balance in dijet, γ+jets and leptonic Z+jets events [23]. These are also propagated to the $p_{\mathrm{T}}^{\mathrm{miss}}$ calculation [24].

Muon candidates within the geometrical acceptance of the silicon tracker and muon subdetectors ($|\eta| < 2.4$) are reconstructed by combining the information from the tracker and the muon chambers [25]. These candidates are required to satisfy a set of quality criteria based on the number of hits measured in the tracker and the muon system, the properties of the fitted muon track, as well as the impact parameters of the track with respect to the primary vertex of the event.

Electron candidates, within $|\eta| < 2.5$, are reconstructed using an algorithm that associates tracks reconstructed in the silicon tracker with electromagnetic energy clusters in the ECAL [26]. To reduce the misidentification rate, these candidates are required to satisfy identification criteria based on the shower shape of the energy deposit, the matching of the electron track to the ECAL energy cluster, the relative amount of energy deposited in the HCAL detector, and the consistency of the electron track with the primary vertex. Electron candidates that are identified as coming from photon conversions in the detector are removed.

Identified electrons or muons are usually expected to be isolated from hadronic activity in the event. The isolation sum is defined by summing the p_{T} of all the PF candidates within a cone of radius 0.4 (0.3) around the muon (electron) track, and is corrected for the contribution of neutral hadrons from pileup interactions. The isolation is required to be smaller than 25% (16%) of the muon (electron) transverse momentum.

Hadronically decaying τ leptons are identified from jets reconstructed through the hadron-plus-strip algorithm [27], that requires a subset of particles inside the jet consistent with the decay products of a τ lepton. In addition, the τ candidate must be isolated from other activity in the detector. The isolation sum is computed by summing the p_{T} of all the charged PF candidates and PF photons within a cone of radius 0.3 around the jet axis. Hadronic τ leptons are selected with an average efficiency of about 70%.

4 Event simulation

The signal and background processes are simulated using several Monte Carlo (MC) generators. The Higgs boson signal events produced through ggH and qqH are generated with POWHEG 2.0 [28–32], at next-to-leading order (NLO) in quantum chromodynamics (QCD). Signal events are normalized to the inclusive Higgs boson production cross sections taken from the recommendations of Ref. [33]. The ggH production cross section is computed at next-to-next-to-next-to leading order ($\mathrm{N^3LO}$) precision in QCD, and at NLO in electroweak (EW) corrections [34]. The cross section for the Higgs boson production through VBF is calculated at next-to-next-to leading order (NNLO) in QCD, including both the next-to-next-to leading logarithmic (NNLL) QCD and NLO EW corrections. The ggH process is simulated using calculations in which the top quark loop is fully resolved. Moreover, the p_{T} distribution of the Higgs boson produced via ggH is reweighted to match the NNLO+NNLL prediction from HRES2.1 [35, 36]. Both ggH and qqH signal events are generated assuming a Higgs boson mass of 125 GeV, which is consistent with the combined ATLAS and CMS measurement [37].

The $Z/\gamma^*(\ell^+\ell^-)$ + jets, $\mathrm{Z}(\nu\bar{\nu})$+jets, and $\mathrm{W}(\ell\nu)$+jets backgrounds are simulated at leading order (LO) using MADGRAPH5_aMC@NLO [38], where up to four partons in the final state are

included in the matrix element calculation. The background processes involving the purely EW production of a vector boson (W or Z) in association with two jets are also simulated at LO via MADGRAPH5_aMC@NLO, with up to two partons in the final state. The QCD multijet background is also simulated at LO using MADGRAPH5_aMC@NLO. The $\mathrm{t\bar{t}}$ and single top quark background samples are produced at NLO QCD using POWHEG. Finally, the WZ and ZZ diboson productions are simulated at LO with PYTHIA 8.205 [39], while the Vγ and WW processes are simulated at NLO QCD using MADGRAPH5_aMC@NLO and POWHEG, respectively.

In all cases, events produced from matrix elements are interfaced with PYTHIA 8.205 or higher for the simulation of fragmentation, parton showering, hadronization, and the underlying event description, using the parameters from the CUETP8M1 tune [40]. In the case of the MADGRAPH5_aMC@NLO samples, partons from the matrix element calculation are matched to the parton shower description via the MLM scheme [41]. The NNPDF 3.0 [42] parton distribution functions (PDFs) are used for all the MC samples. Interactions of the final-state particles with the CMS detector are simulated with GEANT4 [43]. Simulated events include the effects of pileup, and are weighted to reproduce the pileup distribution observed in the data.

5 Event selection

At the first trigger level, signal region events are selected using missing transverse momentum based triggers, computed as the vector sum of the p_{T} of all the energy depositions in the calorimeters with $|\eta| < 3$, whose thresholds vary between 60 and 90 GeV, depending on the instantaneous luminosity. Moreover, at the HLT, events of interest are collected using triggers with thresholds of 110 or 120 GeV, depending on the data taking period, applied equally to both the missing transverse momentum ($p_{\mathrm{T,trig}}^{\mathrm{miss}}$), computed as the magnitude of the vector sum of the p_{T} of all the particles reconstructed at the trigger level, and the $H_{\mathrm{T,trig}}^{\mathrm{miss}}$ variable, defined as the magnitude of the vector sum of the p_{T} of the reconstructed jets in the event. Jets considered in the $H_{\mathrm{T,trig}}^{\mathrm{miss}}$ computation are required to have $p_{\mathrm{T}} > 20$ GeV and $|\eta| < 5$. Moreover, the energy fraction attributed to neutral hadrons in these jets is required to be less than 0.9, to remove spurious reconstructed jets from detector noise. Both $p_{\mathrm{T,trig}}^{\mathrm{miss}}$ and $H_{\mathrm{T,trig}}^{\mathrm{miss}}$ are calculated without including muon candidates, allowing the same set of triggers to be used also for selecting events in the muon control samples, which are used in the background estimation procedure described in Section 6.

Events considered in the VBF search are required to have at least two jets with p_{T} larger than 80 and 40 GeV, respectively. Since the L1 trigger decision does not use information from the hadronic activity in the forward region, at least one of the two leading jets in the event is required to have $|\eta| < 3$. To ensure a high trigger efficiency, events are further required to have $p_{\mathrm{T}}^{\mathrm{miss}} > 250$ GeV. The trigger efficiency is measured as a function of $H_{\mathrm{T}}^{\mathrm{miss}}$, computed from jets with p_{T} larger than 30 GeV and $|\eta| < 3$. These triggers are found to be fully efficient for events passing the analysis selection with $H_{\mathrm{T}}^{\mathrm{miss}} > 250$ GeV. In addition, if the leading jet is within the geometrical acceptance of the tracker, $|\eta| < 2.4$, its energy fraction attributed to charged hadrons must be greater than 10%, while the energy fraction attributed to neutral hadrons must be smaller than 80%. These requirements, along with quality filters applied to tracks, muon candidates, and other physics objects, reduce the background due to large misreconstructed $p_{\mathrm{T}}^{\mathrm{miss}}$ [44] originating from non-collision backgrounds. To further suppress the contamination from QCD multijet events, in which a large $p_{\mathrm{T}}^{\mathrm{miss}}$ may arise from a severe mismeasurement of the jet momentum, the minimum azimuthal angle between the $\vec{p}_{\mathrm{T}}^{\mathrm{miss}}$ vector and the directions of each of the four highest p_{T} jets in the event, with $p_{\mathrm{T}} > 30$ GeV and $|\eta| < 4.7$, is required to be larger than 0.5 radians. This selection reduces the QCD multijet contribution to less than 1%

of the total background.

The two leading jets in VBF signal events typically have a large separation in η, large m_{jj} and a small azimuthal separation ($|\Delta\phi_{jj}|$), as reported in Fig. 9 of the Appendix A. The last of these results from a combination between the spin-parity properties of the Higgs boson and the high p_T regime explored by this search, in which the two VBF jets tend to recoil against the invisible system. The $Z(\nu\bar{\nu})$+jets and $W(\ell\nu)$+jets processes constitute the largest backgrounds in this search. They are suppressed in the cut-and-count analysis by requiring $|\Delta\eta_{jj}| > 4.0$, $m_{jj} > 1.3\,\text{TeV}$, and $|\Delta\phi_{jj}| < 1.5$. The shape analysis employs comparatively relaxed requirements of $|\Delta\eta_{jj}| > 1.0$ and $m_{jj} > 200\,\text{GeV}$, while the $\Delta\phi_{jj}$ selection remains unchanged. The $W(\ell\nu)$+jets background is further suppressed by rejecting events that contain at least one isolated electron or muon with $p_T > 10\,\text{GeV}$, or a hadronically decaying τ lepton with $p_T > 18\,\text{GeV}$ and $|\eta| < 2.3$. To reduce the contribution of the γ + jets and $V\gamma$ processes, events containing an isolated photon with $p_T > 15\,\text{GeV}$ and $|\eta| < 2.5$, passing identification criteria based on its ECAL shower shape [45], are vetoed. Finally, top quark backgrounds ($t\bar{t}$ and single top processes) are suppressed by rejecting events in which a b quark jet, with $p_T > 20\,\text{GeV}$ and $|\eta| < 2.4$, is identified through the combined secondary vertex algorithm [46, 47]. A working point that yields a 60% efficiency for tagging jets from the fragmentation of b quarks, and a 1% probability of misidentifying a light-flavor jet as a b-jet is used.

A summary of the selection criteria for the signal region for both the shape and the cut-and-count analyses is reported in Table 1.

Table 1: Summary of the kinematic selections used to define the signal region for both the shape and the cut-and-count analyses.

Observable	Shape analysis	Cut-and-count analysis	Target background
Leading (trailing) jet	$p_T > 80\,(40)\,\text{GeV}$, $\lvert\eta\rvert < 4.7$		All
p_T^{miss}	$> 250\,\text{GeV}$		QCD multijet, $t\bar{t}$, W + jets
$\Delta\phi(\vec{p}_T^{miss}, \vec{p}_T^{jet})$	< 0.5		QCD multijet
$\lvert\Delta\phi_{jj}\rvert$	< 1.5 radians		$Z(\nu\bar{\nu})$+jets, $W(\ell\nu)$+jets
$\eta_{j1} \cdot \eta_{j2}$	< 0		$Z(\nu\bar{\nu})$+jets, $W(\ell\nu)$+jets
$\lvert\Delta\eta_{jj}\rvert$	> 1	> 4	$Z(\nu\bar{\nu})$+jets, $W(\ell\nu)$+jets
$\lvert m_{jj}\rvert$	$> 200\,\text{GeV}$	$> 1300\,\text{GeV}$	$Z(\nu\bar{\nu})$+jets, $W(\ell\nu)$+jets
Muons and electrons	$N_{\mu,e} = 0$ with $p_T > 10\,\text{GeV}$, $\lvert\eta\rvert < 2.4\,(2.5)$		W + jets, $Z(\ell\ell)$+jets
τ leptons	$N_{\tau_h} = 0$ with $p_T > 18\,\text{GeV}$, $\lvert\eta\rvert < 2.3$		W + jets, $Z(\ell\ell)$+jets
Photons	$N_\gamma = 0$ with $p_T > 15\,\text{GeV}$, $\lvert\eta\rvert < 2.5$		γ+jets, $V\gamma$
B-jets	$N_{jet} = 0$ with $p_T > 20\,\text{GeV}$, CSVv2 > 0.8484		$t\bar{t}$, single top

6 Background estimation

The V+jets processes represent the largest backgrounds in this search, constituting about 95% of the total expected background. A significant fraction of the V+jets events can be attributed to the EW production of a Z or a W boson in association with two jets. These processes are referred to as the V+jets (EW) backgrounds. The remaining V+jets contributions arise from the production of a vector boson in association with jets from QCD radiation, and they are referred to as the V+jets (QCD) backgrounds. The V+jets (EW) processes are kinematically similar to VBF Higgs boson signal events, with the two leading jets tending to have large values of $\Delta\eta_{jj}$ and m_{jj}. Therefore, the contribution from V+jets (EW) production increases as a function of m_{jj}. They represent about 2% of the total V+jets background for m_{jj} around 200 GeV, increasing to about 20% for m_{jj} around 1.5 TeV, and to more than 50% for m_{jj} above 3 TeV.

The V+jets backgrounds are estimated using data from four mutually exclusive control samples, selected from dimuon, dielectron, single-muon and single-electron events. In these control samples, the $p_{\mathrm{T}}^{\mathrm{miss}}$ is calculated by excluding the p_{T} of the identified leptons. Therefore, it corresponds to the p_{T} of the hadronic recoil system, which resembles the $p_{\mathrm{T}}^{\mathrm{miss}}$ expected from the V+jets backgrounds in the signal region.

6.1 Control sample definition

Dimuon and single-muon control samples are selected using the same $p_{\mathrm{T}}^{\mathrm{miss}}$ triggers that are used to collect events in the signal region. Dimuon events are required to contain exactly two oppositely charged muons with $p_{\mathrm{T}} > 10\,\mathrm{GeV}$, with an invariant mass ($m_{\mu\mu}$) between 60 and 120 GeV, i.e. compatible with a Z boson decay. Events with an additional muon, electron or photon are rejected. At least one of the two muons must have $p_{\mathrm{T}} > 20\,\mathrm{GeV}$, and is required to pass tighter identification criteria based on the number of measurements in the tracker and the muon systems, the quality of the muon track fit, and the consistency of the muon track with the primary vertex. Moreover, the isolation sum, calculated as described in Section 3, is required to be smaller than 15% of the muon p_{T}. These tightly identified muons are selected with an average efficiency of 90%.

In the single-muon control region, events are required to contain exactly one muon with $p_{\mathrm{T}} > 20\,\mathrm{GeV}$, passing both tight identification and isolation requirements. The transverse mass (m_{T}) of the muon-$p_{\mathrm{T}}^{\mathrm{miss}}$ system is computed as $m_{\mathrm{T}}^2 = 2p_{\mathrm{T}}^{\mathrm{miss}}p_{\mathrm{T}}^{\mu}(1-\cos\Delta\phi)$, where p_{T}^{μ} is the p_{T} of the muon, and $\Delta\phi$ is the angle between $\vec{p}_T^{\,\mu}$ and $\vec{p}_{\mathrm{T}}^{\mathrm{miss}}$. No additional muon, electron or photon is allowed, and the transverse mass must be smaller than 160 GeV. Dimuon and single-muon events are further required to fulfill all the other selections imposed on events in the signal region, where the $p_{\mathrm{T}}^{\mathrm{miss}}$ is replaced by the p_{T} of the hadronic recoil system.

Dielectron and single-electron control samples are defined using events collected mainly by a single-electron trigger with a p_{T} threshold of 27 GeV. In events where the Z boson has $p_{\mathrm{T}} > 600\,\mathrm{GeV}$, the two electrons produced in the decay have a small angular separation, to the point that they can be included in each other's isolation cones. This results in an inefficiency for the chosen trigger, which imposes isolation requirements on electron candidates. This inefficiency is mitigated by including events collected by a single-electron trigger with a p_{T} threshold of 105 GeV and no isolation requirements on the electron candidate. The dielectron control sample is selected from events containing exactly two oppositely charged electrons with $p_{\mathrm{T}} > 10\,\mathrm{GeV}$, and no additional muon, electron or photon. The invariant mass of the dielectron system is required to be between 60 and 120 GeV, as for the dimuon events. One of the two electrons must have $p_{\mathrm{T}} > 40\,\mathrm{GeV}$, and is required to pass a tight identification criterion based on the shower shape of its ECAL energy deposit, the matching of the electron track to the ECAL energy cluster, and the consistency of the electron track with the primary vertex. Furthermore, the isolation sum, calculated as described in Section 3, is required to be smaller than 6% of the electron p_{T}.

Events in the single-electron control sample are required to contain exactly one tightly identified and isolated electron with $p_{\mathrm{T}} > 40\,\mathrm{GeV}$. No additional muons, electrons or photons are allowed. The contamination from QCD multijet events is reduced by requiring $p_{\mathrm{T}}^{\mathrm{miss}} > 60\,\mathrm{GeV}$ and $m_{\mathrm{T}} < 160\,\mathrm{GeV}$.

6.2 V+jets background estimation

The procedure for estimating the V+jets backgrounds relies on "transfer factors" derived from simulation, which are used to derive the background estimates in the signal region from the

V+jets yield in the control sample. In the cut-and-count analysis, the number of observed events in each control sample is used to predict the V+jets backgrounds in the signal region. In contrast, in the shape analysis, the m_{jj} distributions in the control sample are used to estimate the m_{jj} spectrum of the V+jets backgrounds in the signal region.

The transfer factors for the dilepton control samples use the $\mathrm{Z}(\mu\mu)$+jets and the $\mathrm{Z}(\mathrm{ee})$+jets event yields to determine the $\mathrm{Z}(\nu\bar{\nu})$+jets background yield in the signal region. They account for the difference in the branching fractions of $\mathrm{Z}(\nu\bar{\nu})$ and $\mathrm{Z}(\ell\ell)$ decays, as well as the impact of lepton acceptance and selection efficiencies. In the case of dielectron events, the transfer factors also account for the difference in trigger efficiencies. The resulting constraint on the $\mathrm{Z}(\nu\bar{\nu})$+jets processes from the dilepton regions is limited by the statistical uncertainty of the dilepton control samples because of the large difference in the branching fractions between $\mathrm{Z}(\nu\bar{\nu})$ and $\mathrm{Z}(\ell\ell)$ decays. Transfer factors are also defined between the $\mathrm{W}(\mu\nu)$+jets and the $\mathrm{W}(\mathrm{e}\nu)$+jets event yields in the single-lepton control samples and the $\mathrm{W}(\ell\nu)$+jets background contribution in the signal region. These take into account the effect of lepton acceptance, selection efficiencies, lepton and hadronic τ veto efficiencies, as well as the difference in trigger efficiencies in the case of the single-electron control sample.

Finally, to profit from the larger statistical power of the $\mathrm{W}(\mu\nu)$+jets and $\mathrm{W}(\mathrm{e}\nu)$+jets control regions, transfer factors are also defined to estimate the $\mathrm{Z}(\nu\bar{\nu})$+jets and $\mathrm{W}(\ell\nu)$+jets yields in the signal region providing an additional constraint in the $\mathrm{Z}(\nu\bar{\nu})$+jets background measurement. These transfer factors rely on an accurate prediction of the ratio of V+jets (QCD) and V+jets (EW) processes. Therefore, the LO simulations for the $\mathrm{Z}+\mathrm{jets}$ (QCD) and the $\mathrm{W}+\mathrm{jets}$ (QCD) processes are corrected using boson p_{T} and m_{jj} dependent NLO QCD k-factors derived with MADGRAPH5_aMC@NLO. Furthermore, $\mathrm{Z}+\mathrm{jets}$ and $\mathrm{W}+\mathrm{jets}$ simulations are also corrected with NLO EW k-factors, derived from theoretical calculations [48–50], as a function of boson p_{T}. Similarly, $\mathrm{Z}+\mathrm{jets}$ (EW) and $\mathrm{W}+\mathrm{jets}$ (EW) processes are corrected with NLO QCD k-factors derived through the VBFNLO event generator [51, 52] as a function of boson p_{T} and m_{jj}.

The V+jets background yields are determined through a maximum-likelihood fit, performed simultaneously across all the control samples and the signal region. The likelihood function ($\mathcal{L}$) is defined as:

$$
\begin{aligned}
\mathcal{L}(\mu, \boldsymbol{\kappa}^{\mathbf{Z}(\nu\bar{\nu})}, \boldsymbol{\theta}) = & \prod_i \mathrm{Pois}\left(d_i | B_i(\boldsymbol{\theta}) + (1 + f_i(\boldsymbol{\theta})_{\mathrm{QCD}})\boldsymbol{\kappa}_i^{\mathrm{Z}(\nu\bar{\nu})} + R_i^{\mathrm{Z}}(1 + f_i(\boldsymbol{\theta})_{\mathrm{EW}})\boldsymbol{\kappa}_i^{\mathrm{Z}(\nu\bar{\nu})} + \mu S_i(\boldsymbol{\theta})\right) \times \\
& \prod_i \mathrm{Pois}\left(d_i^{\mu\mu} | B_i^{\mu\mu}(\boldsymbol{\theta}) + \frac{\boldsymbol{\kappa}_i^{\mathrm{Z}(\nu\bar{\nu})}}{R_i^{\mu\mu}(\boldsymbol{\theta})_{\mathrm{QCD}}} + \frac{R_i^{\mathrm{Z}}\boldsymbol{\kappa}_i^{\mathrm{Z}(\nu\bar{\nu})}}{R_i^{\mu\mu}(\boldsymbol{\theta})_{\mathrm{EW}}}\right) \\
& \prod_i \mathrm{Pois}\left(d_i^{\mathrm{ee}} | B_i^{\mathrm{ee}}(\boldsymbol{\theta}) + \frac{\boldsymbol{\kappa}_i^{\mathrm{Z}(\nu\bar{\nu})}}{R_i^{\mathrm{ee}}(\boldsymbol{\theta})_{\mathrm{QCD}}} + \frac{R_i^{\mathrm{Z}}\boldsymbol{\kappa}_i^{\mathrm{Z}(\nu\bar{\nu})}}{R_i^{ee}(\boldsymbol{\theta})_{\mathrm{EW}}}\right) \times \\
& \prod_i \mathrm{Pois}\left(d_i^{\mu} | B_i^{\mu}(\boldsymbol{\theta}) + \frac{f_i(\boldsymbol{\theta})_{\mathrm{QCD}}\,\boldsymbol{\kappa}_i^{\mathrm{Z}(\nu\bar{\nu})}}{R_i^{\mu}(\boldsymbol{\theta})_{\mathrm{QCD}}} + \frac{R_i^{\mathrm{Z}} f_i(\boldsymbol{\theta})_{\mathrm{EW}}\,\boldsymbol{\kappa}_i^{\mathrm{Z}(\nu\bar{\nu})}}{R_i^{\mu}(\boldsymbol{\theta})_{\mathrm{EW}}}\right) \times \\
& \prod_i \mathrm{Pois}\left(d_i^{e} | B_i^{e}(\boldsymbol{\theta}) + \frac{f_i(\boldsymbol{\theta})_{\mathrm{QCD}}\,\boldsymbol{\kappa}_i^{\mathrm{Z}(\nu\bar{\nu})}}{R_i^{\mu}(\boldsymbol{\theta})_{\mathrm{QCD}}} + \frac{R_i^{\mathrm{Z}} f_i(\boldsymbol{\theta})_{\mathrm{EW}}\,\boldsymbol{\kappa}_i^{\mathrm{Z}(\nu\bar{\nu})}}{R_i^{e}(\boldsymbol{\theta})_{\mathrm{EW}}}\right)
\end{aligned}
\tag{1}
$$

where $\mathrm{Pois}(x|y) = y^x \mathrm{e}^{-y}/x!$. The symbol i denotes each bin of the m_{jj} distribution in the shape analysis while, in the cut-and-count analysis, i stands for a single bin that represents the event yields obtained at the end of the event selection. The symbols $d_i^{\mu\mu}$, d_i^{ee}, d_i^{μ}, d_i^{e}, and d_i denote the observed number of events in each bin i of the dimuon, dielectron, single-muon, single-electron and signal regions, respectively. The symbols $f_i(\boldsymbol{\theta})_{\mathrm{QCD}}$ and $f_i(\boldsymbol{\theta})_{\mathrm{EW}}$ indicate the

ratios between the $Z(\nu\bar{\nu})$+jets and $W(\ell\nu)$+jets backgrounds in the signal region from QCD and EW production, respectively. The symbols $R_i^{\mu\mu}(\boldsymbol{\theta})_{\mathrm{QCD}}$, $R_i^{\mathrm{ee}}(\boldsymbol{\theta})_{\mathrm{QCD}}$, $R_i^{\mu}(\boldsymbol{\theta})_{\mathrm{QCD}}$, and $R_i^{\mathrm{e}}(\boldsymbol{\theta})_{\mathrm{QCD}}$ are the transfer factors relating the dimuon, dielectron, single-muon, and single-electron control samples, respectively, to the signal region for the V+jets (QCD) processes. Similarly, $R_i^{\mu\mu}(\boldsymbol{\theta})_{\mathrm{EW}}$, $R_i^{\mathrm{ee}}(\boldsymbol{\theta})_{\mathrm{EW}}$, $R_i^{\mu}(\boldsymbol{\theta})_{\mathrm{EW}}$, and $R_i^{\mathrm{e}}(\boldsymbol{\theta})_{\mathrm{EW}}$ indicate the transfer factors for the V+jets (EW) processes. The parameters $\boldsymbol{\kappa}_i^{\mathrm{Z}(\nu\bar{\nu})}$ represent the yield of the $Z(\nu\bar{\nu})$+jets (QCD) background in each bin i of the signal region, and are left to float freely in the fit. In a given bin, the $Z(\nu\bar{\nu})$+jets (EW) background yield is obtained from $\boldsymbol{\kappa}_i^{\mathrm{Z}(\nu\bar{\nu})}$ through the transfer factor R_i^{Z}, that represents the ratio between the $Z(\nu\bar{\nu})$+jets (QCD) and $Z(\nu\bar{\nu})$+jets (EW) processes. The contributions from subleading background processes are denoted by $B_i^{\mu\mu}$, B_i^{ee}, B_i^{μ}, B_i^{e} and B_i, respectively. Finally, the likelihood also includes a signal term in which S_i represents the expected signal prediction, while $\mu = \sigma\mathcal{B}(\mathrm{H} \to \mathrm{inv})/\sigma_{\mathrm{SM}}$ denotes the signal strength parameter.

Systematic uncertainties are modelled as constrained nuisance parameters ($\boldsymbol{\theta}$). In particular, the uncertainties in the $Z(\nu\bar{\nu})$+jets and $W(\ell\nu)$+jets backgrounds enter in the likelihood as variations of the transfer factors. These include theoretical uncertainties in the Z + jets to W + jets differential cross section ratio, for both QCD and EW processes, due to the choice of the renormalization and the factorization scales, as well as the uncertainties on the PDFs. Scale variations are assumed to be uncorrelated between the Z + jets and W + jets processes, therefore they do not cancel in the Z + jets to W + jets ratio. This results in larger uncertainties compared to those recommended in Ref. [53] ranging, as a function of m_{jj}, between 8 and 12% from renormalization scale variations, and between 2 and 7% from factorization scale variations, for both Z + jets/W + jets (QCD) and (EW) ratios. This conservative approach accounts also for the unknown effect of the interference between the V+jets (QCD) and V+jets (EW) processes, which is not included in the simulation. In contrast, the PDF uncertainties are assumed to be correlated across V+jets processes, resulting in a residual uncertainty smaller than 1% on Z + jets/W + jets ratios. Moreover, the uncertainties related to NLO EW corrections to the V+jets (QCD) processes are estimated according to the recommendations in Ref. [53], and are found to be about 1–2% across the entire m_{jj} spectrum. Additional uncertainties are included, namely: the uncertainties in the reconstruction efficiencies of leptons (around 1% per muon or electron), the selection efficiencies of leptons (about 1% per muon, 1.5% per electron), the veto efficiency of leptons (around 2% per muon, 1% per electron) and hadronically decaying τ leptons (about 3.5% per τ), the knowledge of the jet energy scale (1–2%), and the efficiency of the electron (around 1%) and $p_{\mathrm{T}}^{\mathrm{miss}}$ (about 2%) triggers.

The full set of systematic uncertainties related to the V+jets transfer factors are listed in Table 2. Before the fit, the total uncertainty in the background estimation in the signal region ranges between 4.5 and 6% as a function of m_{jj}, dominated by the theoretical uncertainties in the Z + jets to W + jets cross section ratio for both QCD and EW production. The impact of each source of systematic uncertainty, as reported in Table 2 in the context of the shape analysis, is defined as the maximum difference in the fitted value of the signal strength, $\sigma\mathcal{B}(\mathrm{H} \to \mathrm{inv})/\sigma_{\mathrm{SM}}$, obtained when varying the associated nuisance parameter within one standard deviation of its maximum likelihood estimate.

Finally, to assess the level of agreement between data and MC obtained through the application of p_{T}–m_{jj} dependent NLO corrections for both V+jets (QCD) and V+jets (EW) productions, the ratio between the number of Z + jets and W + jets events in the control samples in bins of m_{jj} is used as figure of merit, as shown in Fig. 10 of the Appendix A. Good agreement is observed between data and simulation and local differences are covered by the systematic uncertainties on the ratios listed in Table 2.

Table 2: Experimental and theoretical sources of systematic uncertainties on the V+jets transfer factors, which enter in the simultaneous fit used to estimate V+jets (QCD) and V+jets (EW) backgrounds as constrained nuisance parameters. In addition, the impact on the fitted signal strength, $\sigma\mathcal{B}(\mathrm{H} \to \mathrm{inv})/\sigma_{\mathrm{SM}}$, is also reported in the last column after performing the m_{jj} shape analysis fit to the observed data across signal and control regions.

Source of uncertainty	Ratios	Uncertainty vs m_{jj}	Impact on $\mathcal{B}(\mathrm{H} \to \mathrm{inv})$
Theoretical uncertainties			
Ren. scale V+jets (EW)	$Z(\nu\nu)/W(\ell\nu)$ (EW)	9–12%	48%
Ren. scale V+jets (QCD)	$Z(\nu\nu)/W(\ell\nu)$ (QCD)	9–12%	23%
Fac. scale V+jets (EW)	$Z(\nu\nu)/W(\ell\nu)$ (EW)	2–7%	4%
Fac. scale V+jets (QCD)	$Z(\nu\nu)/W(\ell\nu)$ (QCD)	2–7%	2%
PDF V+jets (QCD)	$Z(\nu\nu)/W(\ell\nu)$ (QCD)	0.5–1%	$< 1\%$
PDF V+jets (EW)	$Z(\nu\nu)/W(\ell\nu)$ (EW)	0.5–1%	$< 1\%$
NLO EW corr.	$Z(\nu\nu)/W(\ell\nu)$ (QCD)	1–2%	$< 1\%$
Experimental uncertainties			
Muon reco. eff.	$W(\mu\nu)/W(\ell\nu)$, $Z(\mu\mu)/Z(\nu\nu)$	$\approx 1\%$ (per leg)	8%
Ele. reco. eff.	$W(e\nu)/W(\ell\nu)$, $Z(ee)/Z(\nu\nu)$	$\approx 1\%$ (per leg)	3%
Muon id. eff.	$W(\mu\nu)/W(\ell\nu)$, $Z(\mu\mu)/Z(\nu\nu)$	$\approx 1\%$ (per leg)	8%
Ele. id. eff.	$W(e\nu)/W(\ell\nu)$, $Z(ee)/Z(\nu\nu)$	$\approx 1.5\%$ (per leg)	4%
Muon veto	$W(CRs)/W(\ell\nu)$, $Z(\nu\nu)/W(\ell\nu)$	≈ 2.5 (2)% for EW (QCD)	7%
Ele. veto	$W(CRs)/W(\ell\nu)$, $Z(\nu\nu)/W(\ell\nu)$	≈ 1.5 (1)% for EW (QCD)	5%
τ veto	$W(CRs)/W(\ell\nu)$, $Z(\nu\nu)/W(\ell\nu)$	≈ 3.5 (3)% for EW (QCD)	13%
Jet energy scale	$Z(CRs)/Z(\nu\nu)$, $W(CRs)/W(\ell\nu)$	≈ 1 (2)% for Z/Z (W/W)	2%
Ele. trigger	$W(e\nu)/W(\ell\nu)$, $Z(ee)/Z(\nu\nu)$	$\approx 1\%$	$< 1\%$
$p_{\mathrm{T}}^{\mathrm{miss}}$ trigger	All ratios	$\approx 2\%$	18%

6.3 Minor backgrounds

In addition to the V+jets processes, several other sources of background contribute to the total event yield in the signal region. These include QCD multijet events that typically have small genuine $p_{\mathrm{T}}^{\mathrm{miss}}$. However, jet momentum mismeasurement and instrumental effects may give rise to large $p_{\mathrm{T}}^{\mathrm{miss}}$ tails. A $\Delta\phi$ extrapolation method [54] is used to estimate this background from data, where a QCD multijet enriched control sample is obtained by selecting events that fail the $\Delta\phi$ requirement between the jets and the $\vec{p}_{\mathrm{T}}^{\mathrm{miss}}$ vector, but still fulfill the remaining event selection criteria. A transfer factor, derived from simulated QCD multijet events, is used to estimate the background in the signal region from the event rate measured in the low-$\Delta\phi$ sample. The low-$\Delta\phi$ region contains a significant contamination from V+jets production, which have genuine $p_{\mathrm{T}}^{\mathrm{miss}}$. They contribute about 40% in the total event yield for m_{jj} smaller than 500 GeV, and about 80% for $m_{\mathrm{jj}} > 3$ TeV. This contamination is estimated from simulation and subtracted from the event yield measured in the low-$\Delta\phi$ sample. An uncertainty of 20% is assigned while performing the subtraction, which results in an uncertainty of about 30% in the estimated QCD multijet background in the signal region. The MC statistical uncertainty of the QCD multijet samples, which affects the transfer factor prediction, is also considered and is found to vary between 40–100% as a function of m_{jj}. Lastly, a validation of this $\Delta\phi$ method is performed using a purer sample of QCD multijet events that pass the analysis requirements but have $p_{\mathrm{T}}^{\mathrm{miss}}$ in the range between 100–175 GeV. In this validation region, the predicted QCD background is found to agree with the observation within 50%, which is taken as an additional conservative uncertainty.

The remaining background sources include top quark production and diboson (VV) processes, which are estimated directly from simulation. The p_{T} distribution of the top quark in simulated events is corrected to match the observed p_{T} distribution in data [55]. An uncertainty of about 10% is assigned to the overall top quark background normalization, while an additional 10% uncertainty is added to account for the modelling of the top quark p_{T} distribution in simulation.

The overall normalization of the diboson background has an uncertainty of about 15% [56, 57]. The uncertainties in the top quark and diboson backgrounds are correlated across signal and control samples. Moreover, several experimental sources of uncertainty are assigned to the backgrounds estimated from simulation. An uncertainty of 2.5% in the integrated luminosity measurement [58] is propagated to the background yields. The uncertainty in the efficiency of the b-jet veto is estimated to be around 3% for the top quark background and $\approx 1\%$ for the other simulated processes. The uncertainty related to the jet energy scale varies between 8–15% depending on both the process and the control sample.

7 Results

Figures 2–3 show the results of the shape analysis in the four control samples. Data in the signal region data are not included in the simultaneous fit, therefore this represents a pure measurement of the V+jets backgrounds based only on the control samples. This result is referred to as the "control-region-only fit". The data in the control samples are compared to both the pre-fit predictions from simulation and the post-fit estimates obtained after performing the fit. In these figures, the last bin includes all the events with m_{jj} larger than 3.5 TeV. The gray band in the ratio panel indicates the total post-fit uncertainty, which combines the effect of all the systematic uncertainties as well as their correlations. The differences between data and the post-fit background prediction, relative to the quadratic sum of the post-fit uncertainty in the prediction and the statistical uncertainty in the data, are shown in the lowest panel. The control samples with larger statistical power dominate the fit results.

Figure 4 shows the observed and the expected m_{jj} distributions in the signal region, obtained after applying the full event selection. The background prediction shown in Fig. 4 (left) is obtained from a combined fit in all the control samples, excluding the data in the signal region. The estimated event yields for the various SM backgrounds in each m_{jj} bin, obtained after performing the control-region-only fit, are listed in Table 3, along with the observed event yield in the signal region. Expected signal distributions for a Higgs boson decaying exclusively to invisible particles, produced via qqH and ggH modes, are overlaid. Since only an overall normalization discrepancy is observed between the data and the estimated background in the signal region, which is poorly compatible with the presence of invisible Higgs decays, data are in agreement with the SM prediction. The correlations between the predicted background yields in each m_{jj} bin, resulting from the fit to the control regions, are reported in Fig. 11 of the supplementary material in Appendix A. The predicted yields reported in Table 3, along with the correlation matrix, can be used in the simplified likelihood approach detailed in Ref. [59] to reinterpret the analysis results in different models to those presented in this letter. Figure 4 (right) shows the background estimate obtained including events from the signal region in the fit, but assuming the absence of any signal. Such a fit is termed as the "background-only fit". The comparison between the results of this fit with an alternative one, which allows the presence of the signal, is used to set an upper limit on $\mathcal{B}(\mathrm{H} \to \mathrm{inv})$.

Furthermore, the observed event yield obtained after the cut-and-count selection is reported in Table 4, along with the predicted backgrounds in the signal region after a control-region-only fit and the event yields in each control sample. A moderate excess of data is observed in the signal region compared to the background prediction obtained from the control samples. The excess is mainly driven by a discrepancy at low m_{jj}, in the range between 1.3 and 1.5 TeV, and at intermediate $\Delta\eta_{\mathrm{jj}}$ values, $4.5 < \Delta\eta_{\mathrm{jj}} < 5.5$, and is therefore incompatible with the presence of a real VBF signal. In the same m_{jj} range, an excess is also observed in the shape analysis phase space, as shown in Fig. 4. The excess comes entirely from events with large $\Delta\phi(p_{\mathrm{T}}^{\mathrm{miss}}, p_T^{jet})$, thus

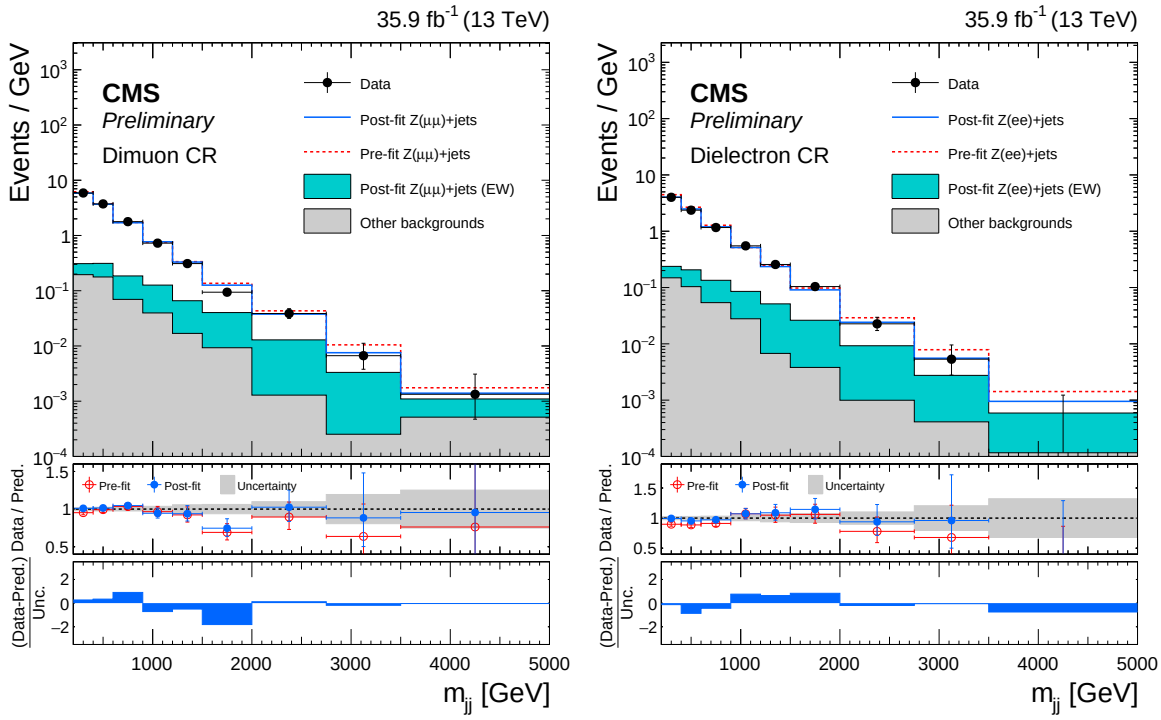

Figure 2: The m_{jj} distributions in the dimuon (left) and dielectron (right) control samples. Data are compared to the simulation, before (dashed red) and after (solid blue) performing the fit. Signal region data are not included in the fit. The filled histograms indicate all processes other than $Z(\ell\ell)$+jets (QCD). The last bin includes all events with $m_{jj} > 3.5$ TeV. Ratios of data and the pre-fit background (red points) and the post-fit background prediction (blue points) are shown. The gray band indicates the overall post-fit uncertainty. The lowest panel shows the distribution of the differences between data and the post-fit background prediction relative to the quadrature sum of the post-fit uncertainty and the statistical uncertainty in data.

Table 3: Expected event yields in each m_{jj} bin for various background processes in the signal region of the shape analysis. The background yields and the corresponding uncertainties are obtained after performing a combined fit to data in all the control samples, but excluding data in the signal region. The "other backgrounds" includes QCD multijet and $Z(\ell\ell)$+jets processes. The expected total signal contribution for the 125 GeV Higgs boson, decaying exclusively to invisible particles, and the observed event yields are also reported.

Process	m_{jj} range in TeV								
	0.2–0.4	0.4–0.6	0.6–0.9	0.9–1.2	1.2–1.5	1.5–2.0	2.0–2.75	2.75–3.5	> 3.5
$Z(\nu\nu)$ (QCD)	9367 ± 394	5716 ± 256	3925 ± 184	1665 ± 84	675 ± 43	406 ± 26	151 ± 14	22.6 ± 3.6	7.5 ± 2.1
$Z(\nu\nu)$ (EW)	202 ± 8	230 ± 10	278 ± 13	203 ± 10	131 ± 8	115 ± 8	71.3 ± 6.6	20.9 ± 3.4	11.6 ± 3.1
$W(\ell\nu)$ (QCD)	4786 ± 252	3046 ± 165	2122 ± 125	936 ± 58	361 ± 29	232 ± 19	79.3 ± 8.9	13.4 ± 2.8	4.3 ± 1.5
$W(\ell\nu)$ (EW)	101 ± 15	118 ± 16	135 ± 18	102 ± 13	61.4 ± 7.9	62.2 ± 7.9	39.9 ± 4.8	13.3 ± 1.8	5.6 ± 1.4
Top-quark	206 ± 32	161 ± 25	124 ± 19	60.7 ± 9.3	31.6 ± 6.1	18.3 ± 2.9	11.1 ± 1.8	2.8 ± 0.5	0.9 ± 0.2
Dibosons	219 ± 39	158 ± 28	119 ± 21	50.9 ± 9.1	19.5 ± 3.5	10.4 ± 1.8	2.8 ± 0.5	1.4 ± 0.3	0.4 ± 0.1
Others	77.5 ± 19.5	51.5 ± 11.5	43.8 ± 10.7	14.3 ± 2.9	6.9 ± 1.5	3.7 ± 0.8	2.5 ± 0.6	0.7 ± 0.3	0.3 ± 0.4
Total Bkg.	14960 ± 563	9482 ± 378	6738 ± 281	3032 ± 135	1286 ± 73	849 ± 48	358 ± 28	75.3 ± 9.8	29.9 ± 7.2
Data	16181	10035	7312	3154	1453	919	411	88	29
Signal	591 ± 285	571 ± 232	566 ± 172	472 ± 131	307 ± 64	344 ± 83	228 ± 40	90.3 ± 18.8	37.4 ± 9.1

it cannot be related to a contamination from instrumental backgrounds since they tend to populate the low $\Delta\phi(p_{\mathrm{T}}^{\mathrm{miss}}, p_T^{jet})$ region. Moreover, as reported in Table 4, the $Z(\nu\bar{\nu})$+jets prediction in the signal region is reduced, compared to the SM expectation, due to a data defict in the dimuon control sample. As shown in Fig. 2 (left), the largest difference is located in the m_{jj}

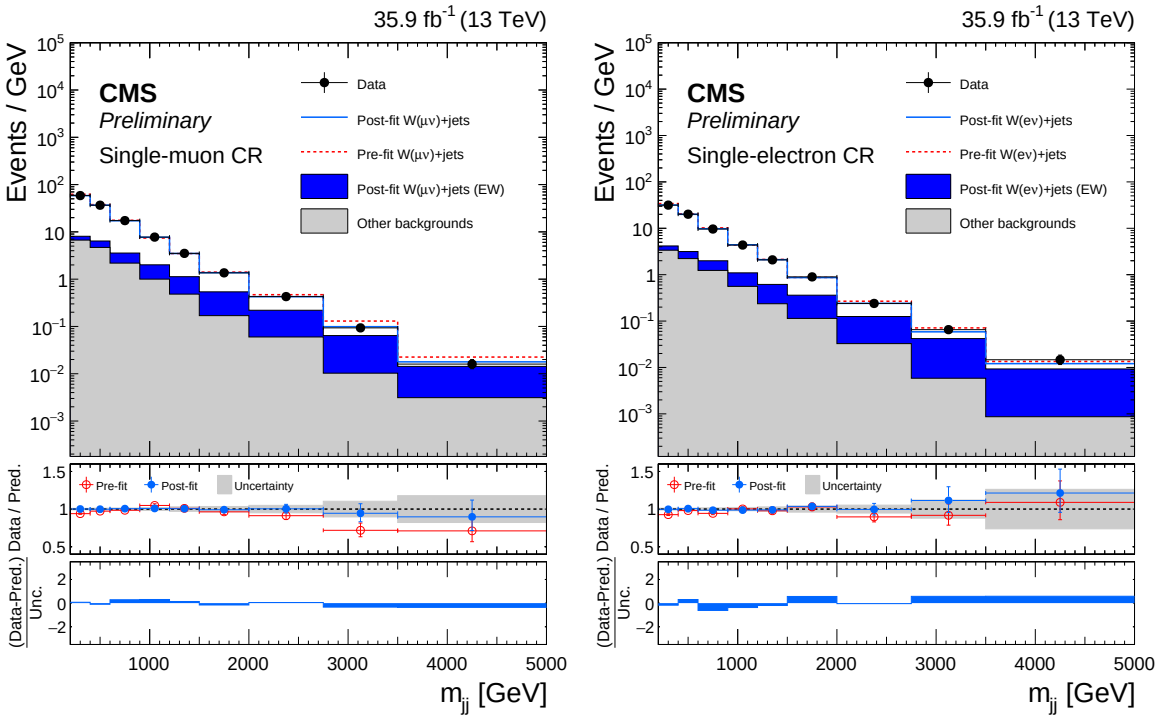

Figure 3: The m_{jj} distributions in the single-muon (left) and single-electron (right) control samples. Data are compared to the simulation, before (dashed red) and after (solid blue) performing the fit. Signal region data are not included in the fit. The filled histograms indicate all processes other than $W(\ell\nu)$+jets (QCD). The last bin includes all events with $m_{jj} > 3.5$ TeV. The description of the lower panels is as in Fig. 2.

region between 1.5 and 2 TeV. Detailed studies have been performed and none of the dimuon sample selections are found to be the cause of this discrepancy. Therefore, the deficit is consistent with being a statistical fluctuation. Figure 5 (left) shows the m_{jj} distribution in the signal region, obtained after applying the cut-and-count selection, where backgrounds are normalized either to the post-fit rate obtained from the control-region-only fit (solid stack) or to the prediction from a background-only fit performed across signal and control regions (dark blue line). Figure 5 (right) shows the same results for the $\Delta\eta_{jj}$ spectrum. Similarly, the observed m_{jj} and $\Delta\eta_{jj}$ distributions in the control regions of the cut-and-count analysis, along with the results obtained from both the control-region-only fit and the background-only one, are reported in Fig. 12, 13, 14 and 15 of the the Appendix A.

7.1 Upper limits on $\mathcal{B}(H \to inv)$

The results of this search are interpreted in terms of an upper limit on the product of the Higgs boson production cross section and its branching fraction to invisible particles, $\sigma\mathcal{B}(H \to inv)$, relative to the predicted cross section assuming SM interactions, σ_{SM}. Observed and expected 95% CL upper limits are computed via an asymptotic approximation of the CL_s method [60, 61], using a profile likelihood ratio test statistic [62] in which systematic uncertainties are modelled as nuisance parameters following a frequentist approach [63]. The profile likelihood ratio is defined as:

$$q = -2\Delta \ln \mathcal{L} = -2 \ln \frac{\mathcal{L}(\text{data}|\sigma\mathcal{B}(H \to inv)/\sigma_{SM}, \hat{\theta}_a)}{\mathcal{L}(\text{data}|\sigma\hat{\mathcal{B}}(H \to inv)/\sigma_{SM}, \hat{\theta})}$$

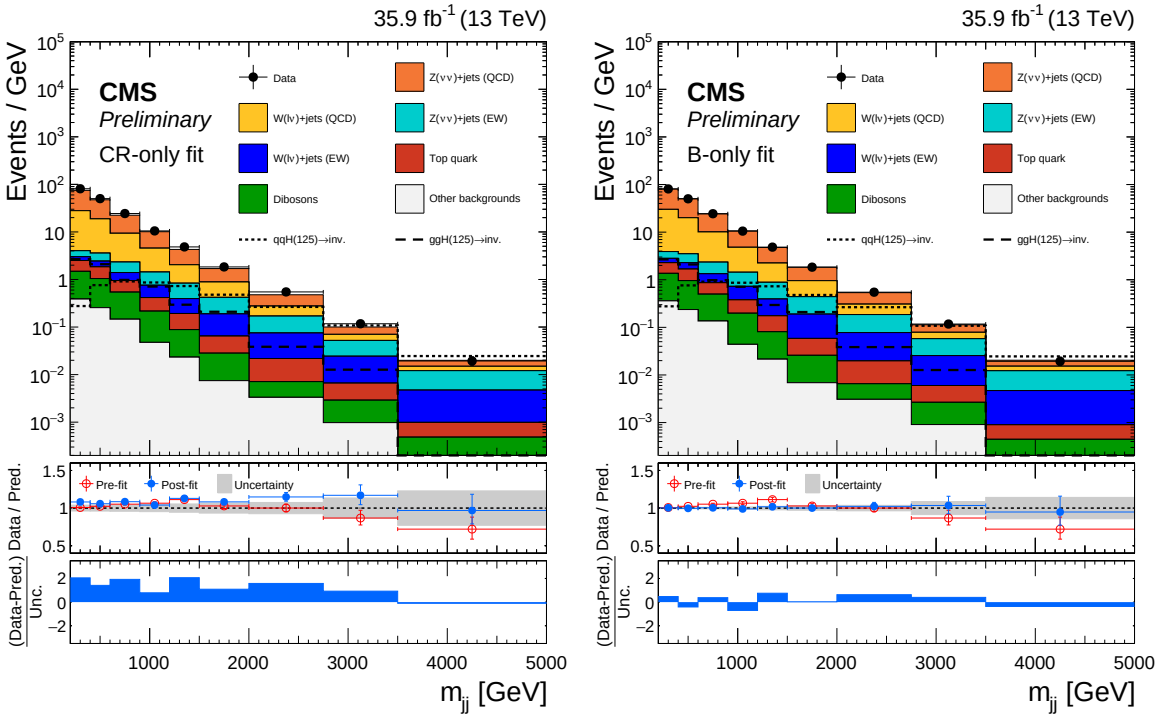

Figure 4: The observed m_{jj} distribution of the shape analysis signal region compared to the post-fit backgrounds from various SM processes. On the left, the predicted backgrounds are obtained from a combined fit to the data in all the control samples but excluding the signal region. On the right, the predicted backgrounds are obtained from a combined fit to the data in all the control samples, as well as in the signal region, assuming the absence of any signal. Expected signal distributions for a 125 GeV Higgs boson produced through ggH and qqH modes, and decaying exclusively to invisible particles, are overlaid. The last bin includes all events with $m_{jj} > 3.5$ TeV. The description of the ratio panels is the same as in Fig. 2.

Table 4: Expected event yields in the signal region and in the control samples of the cut-and-count analysis for various SM processes. The background yields and the corresponding uncertainties are obtained from a combined fit to data in all the control samples, but excluding data in the signal region. The expected total signal contribution for the 125 GeV Higgs boson, decaying exclusively to invisible particles, and the observed event yields are also reported.

Process	Signal Region	Dimuon CR	Dielectron CR	Single-Muon CR	Single-Electron CR
$Z(\nu\nu)$ (QCD)	799 ± 72	-	-	-	-
$Z(\nu\nu)$ (EW)	275 ± 34	-	-	-	-
$Z(\ell\ell)$ (QCD)	-	90.1 ± 7.9	64.7 ± 5.8	26.8 ± 1.2	4.9 ± 0.2
$Z(\ell\ell)$ (EW)	-	32.7 ± 4.3	25.0 ± 3.4	5.9 ± 0.3	2.4 ± 0.2
$W(\ell\nu)$ (QCD)	497 ± 33	0.2 ± 0.2	0.8 ± 0.6	891 ± 31	533 ± 21
$W(\ell\nu)$ (EW)	145 ± 11	0.1 ± 0.1	-	416 ± 16	260 ± 11
Top-quark	43.7 ± 9.8	5.3 ± 1.6	3.7 ± 1.1	126 ± 22	83.1 ± 15.4
Dibosons	19.9 ± 6.1	2.6 ± 1.3	0.9 ± 0.5	23.5 ± 4.9	16.1 ± 4.1
Others	3.3 ± 2.6	-	-	25.6 ± 20.7	2.9 ± 2.9
Total Bkg.	1784 ± 97	131 ± 8	95.2 ± 5.9	1515 ± 34	902 ± 24
Data	2053	114	104	1512	914
Signal $m_{\mathrm{H}} = 125$ GeV	851 ± 148	-	-	-	-

where $\sigma\hat{\mathcal{B}}(\mathrm{H} \to \mathrm{inv})$ represents the value of the signal strength that maximises the likelihood $\mathcal{L}$ for the data, while $\hat{\theta}$ and $\hat{\theta}_a$ denote the best fit estimates for the nuisance parameters and the estimates for a given fixed value of $\sigma\mathcal{B}(\mathrm{H} \to \mathrm{inv})/\sigma_{\mathrm{SM}}$, respectively.

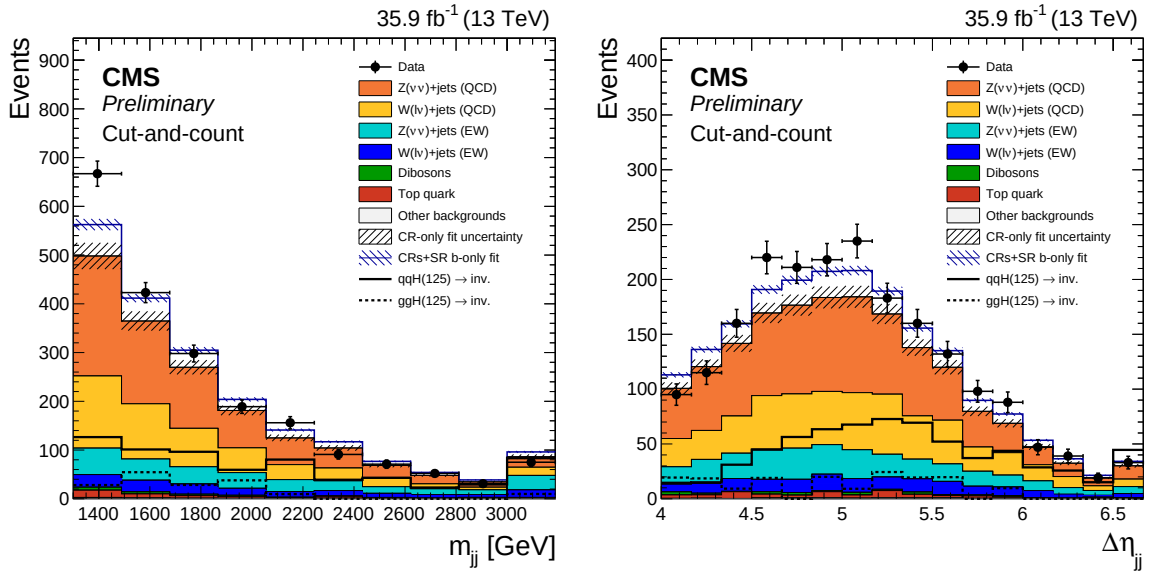

Figure 5: The observed m_{jj} (left) and $\Delta\eta_{jj}$ (right) distributions in the signal region of the cut-and-count analysis compared to the post-fit backgrounds from various SM processes. The predicted background normalizations are obtained either from a combined fit to the data in all the control samples but excluding the signal region (solid stack) or from a background-only fit performed across signal and control regions (dark blue line). Expected signal distributions for a 125 GeV Higgs boson produced through ggH and qqH modes, and decaying exclusively to invisible particles, are overlaid.

Higgs boson production through qqH and ggH mechanisms is considered, and their relative contributions are fixed to the SM prediction within the corresponding uncertainties. The uncertainties in the predictions of the inclusive qqH and ggH production cross sections due to PDF uncertainties, renormalization and factorization scale variations are taken from Ref. [33]. An additional uncertainty of 40% is assigned to the expected ggH contribution. This accounts for both the limited knowledge of the ggH cross section in association with two or more jets, as well as the uncertainty in the prediction of the ggH differential cross section for large Higgs boson transverse momentum, $p_T^H > 250$ GeV. Furthermore, the uncertainties in the signal acceptance due to the choice of the PDFs are evaluated independently for the different signal processes, and are treated as independent nuisance parameters in the fit. The observed (expected) 95% CL upper limit on $\mathcal{B}(\mathrm{H} \to \mathrm{inv})$ is found to be 0.28 (0.21) for the shape analysis, and 0.52 (0.27) in the cut-and-count case. The upper limits are summarized in Table 5. In the cut-and-count analysis, the significance of the excess observed in the signal region, calculated with respect to the background-only hypothesis, is of 2.5σ.

Table 5: Expected and observed 95% CL upper limits on the invisible branching fraction of the Higgs boson, obtained in the shape and cut-and-count analyses. The one and two standard deviation uncertainty range on the expected limits is reported. The signal composition expected in the signal region is also shown.

Analysis	Observed limit	Expected limit	±1 s.d.	±2 s.d.	Signal composition
Shape	0.28	0.21	[0.15–0.29]	[0.11–0.39]	52% qqH, 48% ggH
Cut-and-count	0.53	0.27	[0.20–0.38]	[0.15–0.51]	81% qqH, 19% ggH

7.2 Upper limits on the SM-like Higgs boson scenario

The results presented in Sec. 7.1 are also interpreted in the context of a search for an additional scalar mediator that decays invisibly and interacts with SM particles as the SM Higgs boson. Therefore, the new scalar mediator may be produced via both the ggH and qqH mechanisms and no mixing with the SM Higgs boson is considered. This model has been already benchmarked by several earlier CMS publications [10, 11, 64]. Upper limits computed at 95% CL on $\sigma\mathcal{B}(\mathrm{H} \to \mathrm{inv})/\sigma_{SM}$, are shown in Fig. 6 as a function of the SM-like Higgs boson mass hypothesis (m_{H}) for the both the shape and the cut-and-count analyses.

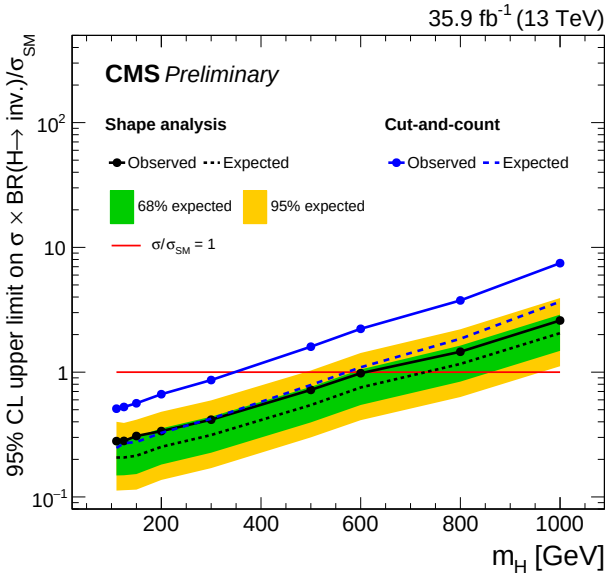

Figure 6: Expected (dashed line) and observed (solid line) 95% CL upper limits on $\sigma\mathcal{B}(\mathrm{H} \to \mathrm{inv})/\sigma_{\mathrm{SM}}$ for a SM-like Higgs boson particle as a function of its mass (m_{H}). Limits are shown for both the shape (black) and the cut-and-count (blue) analyses. The 68 and 95% CL intervals around the expected upper limits for the shape analysis are also reported.

8 Combination of Higgs invisible searches

The common feature of all the searches included in this combination is a large $p_{\mathrm{T}}^{\mathrm{miss}}$, where high p_{T} jets or a weak boson recoil against the invisible particles produced by the Higgs boson decay. Specific topological selections are designed to reduce the contamination from large SM backgrounds, targeting a particular production mode. The analyses included in the combination are listed in Table 6, together with their expected signal composition and their upper limits on $\mathcal{B}(\mathrm{H} \to \mathrm{inv})$.

The results quoted for the VBF channel come from the shape analysis described in this letter, where the large ggH contamination arises from the low m_{jj} region, as shown in Fig. 4. The $\mathrm{Z}(\ell^+\ell^-)\mathrm{H}$ analysis is identical to the one described in Ref. [11], where the expected signal comes entirely from invisible decays of the SM Higgs produced in association with a leptonically decaying Z boson, via either $\mathrm{qq} \to \mathrm{ZH}$ or $\mathrm{gg} \to \mathrm{ZH}$ production. In contrast, the $\mathrm{V}(qq')\mathrm{H}$ and the ggH tagged searches are similar to those described in Ref. [12], but events overlapping with the VBF analysis phase space have been removed to avoid double counting. In both the ggH and $\mathrm{V}(qq')\mathrm{H}$ searches, overlapping events represent 6 (12)% of the total background for a $p_{\mathrm{T}}^{\mathrm{miss}}$ of about 250 (1000) GeV. The overlap removal introduces a 5% loss in the expected exclusion sensitivity compared to Ref. [12]. Both the $\mathrm{V}(qq')\mathrm{H}$ and the ggH searches target events

with at least one high p_T central jet, and their signal regions contain a mixture of different production modes. This mixture results from the limited discrimination power of the substructure observables exploited to select the boosted $V(qq')H$ candidates.

Table 6: Analyses used in this combination, showing final state, expected signal composition along with their observed and expected upper limits on the Higgs invisible branching fraction. The relative contributions assume SM production cross sections.

Analysis	Final state	Signal composition	Observed limit	Expected limit
qqH-tagged	VBF-jets + p_T^{miss}	52% qqH, 48% ggH	0.28	0.21
VH-tagged	$Z(\ell\ell) + p_T^{miss}$ [11]	79% qqZH, 21% ggZH	0.40	0.42
	$V(qq') + p_T^{miss}$ [12]	39% ggH, 6% qqH, 33% WH, 22% ZH	0.50	0.48
ggH-tagged	jets + p_T^{miss} [12]	80% ggH, 12% qqH, 5% WH, 3% ZH	0.66	0.59

No significant deviations from the SM expectations are observed in any of the searches, therefore results are interpreted as an upper limit on $\mathcal{B}(H \to inv)$. These limits are calculated following the same approach described in Section 7.1. The combined likelihood fit accounts for correlations between the nuisance parameters in each search. The uncertainties in the diboson background (except for the $Z(\ell\ell)H$ channel), $t\bar{t}$ and single-top cross sections, lepton efficiencies, momentum scales, integrated luminosity, b-jet and hadronic τ lepton vetoes are correlated among all the searches. In addition, the uncertainties on the inclusive signal production cross sections, due to renormalization/factorization scale variations and PDF uncertainties, are also correlated across the categories. In contrast, since the jet kinematics in the VBF search differ from those in the other analyses, jet energy scale and resolution uncertainties are correlated only across the ggH and VH tagged categories. Finally, theoretical uncertainties applied to the V+jets (QCD) ratios are assumed to be uncorrelated between the VBF analysis and the other searches. The correlation schema applied in the combination is summarized in Table 7 of the supplementary material in Appendix A.

Observed and expected upper limits on $\sigma\mathcal{B}(H \to inv)/\sigma_{SM}$ are computed at 95% CL and are presented in Fig. 7 (left). Assuming SM cross sections for each production mode, the combination yields an observed (expected) upper limit of $\mathcal{B}(H \to inv) < 0.24\ (0.18)$. The profile likelihood ratios as a function of $\mathcal{B}(H \to inv)$, for both the combined fit and each individual search channel, are reported in Fig. 7 (right). Results are shown for both data and an Asimov dataset [62], defined by fixing the nuisances parameters to their maximum likelihood estimate obtained from a fit to the data in which $\mathcal{B}(H \to inv) = 0$ is assumed.

8.1 Non SM production and DM interpretation

The relative sensitivity of each search considered in the combination depends on the assumed SM production rates. The cross section for ggH, qqH and VH production modes are parametrized in terms of coupling strength modifiers κ_V and κ_F, which directly scale the coupling of the Higgs boson to vector bosons and fermions, respectively [65]. The contribution from the gg $\to$ ZH production is scaled to account for the interference between the tH and ZH diagrams, as described in Ref. [33]. In this context, SM production rates are obtained for $\kappa_V = \kappa_F = 1$. Figure 8 (left) shows the observed 95% CL upper limits on $\mathcal{B}(H \to inv)$ evaluated as a function of κ_V and κ_F. The LHC best estimates for κ_V and κ_F from Ref. [4] are superimposed, along with the 68 and 95% CL limit contours. Within the 95% CL region, the observed upper limit on $\mathcal{B}(H \to inv)$ varies between 0.17 and 0.29.

The upper limit on $\mathcal{B}(H \to inv)$, obtained from the combination of the searches listed in Table 6, is interpreted in the context of Higgs-portal models of DM interactions, in which a stable DM particle couples to the SM Higgs boson. Direct detection experiments are sensitive to the

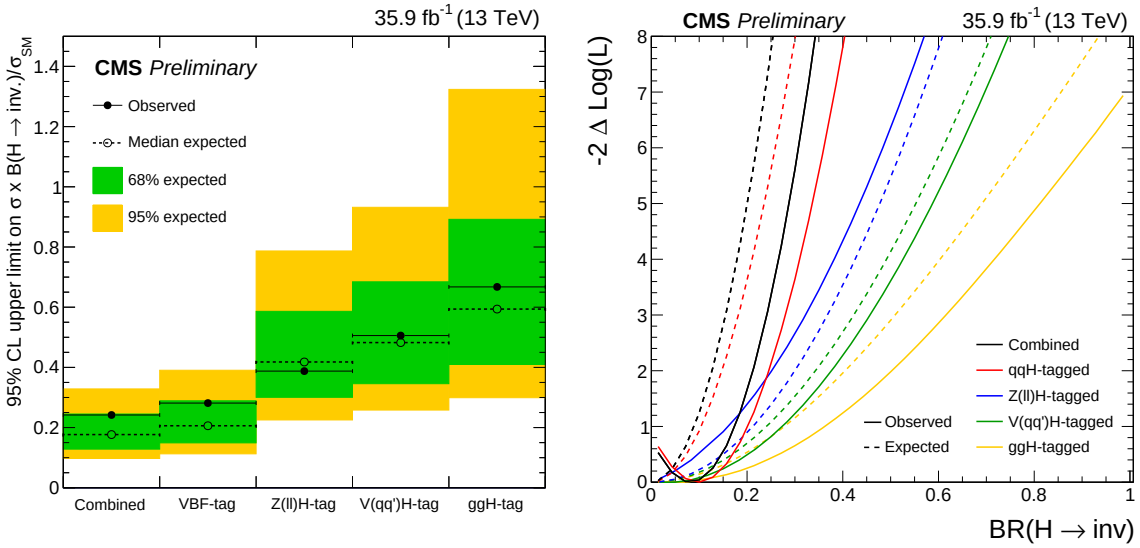

Figure 7: On the left, observed and expected 95% CL upper limits on $\sigma\mathcal{B}(\mathrm{H} \to \mathrm{inv})/\sigma_{\mathrm{SM}}$ for both individual categories targeting qqH, $\mathrm{Z}(\ell\ell)\mathrm{H}$, $\mathrm{V}(qq')\mathrm{H}$ and ggH production model, as well as their combination, assuming a SM Higgs boson with a mass of 125 GeV. On the right, profile likelihood ratios as a function of $\mathcal{B}(\mathrm{H} \to \mathrm{inv})$. The solid curves represent the observations in data, while the dashed lines represent the expected result assuming the absence of any signal. The observed and expected likelihood scans are reported for the full combination, as well as for the individual qqH, $\mathrm{Z}(\ell\ell)\mathrm{H}$, $\mathrm{V}(qq')\mathrm{H}$ and ggH tagged analyses.

interaction between a DM particle and atomic nuclei, which may be mediated by the exchange of a Higgs boson, producing nuclear recoil signatures that can be interpreted in terms of the DM-nucleon scattering cross section. The sensitivity of these experiments depends mainly on the DM particle mass (m_χ). If m_χ is smaller than half of the Higgs boson mass, the Higgs boson invisible width (Γ_{inv}) can be translated, within an effective field theory approach, into a spin-independent DM-nucleon elastic scattering cross section, as outlined in Ref. [9]. This translation is performed assuming that the DM candidate is either a scalar or a fermion; the dimensionless nuclear form-factor f_N is assumed to be equal to 0.326 [66]. The conversion from $\mathcal{B}(\mathrm{H} \to \mathrm{inv})$ to Γ_{inv} uses the relation $\mathcal{B}(\mathrm{H} \to \mathrm{inv}) = \Gamma_{\mathrm{inv}}/(\Gamma_{\mathrm{SM}} + \Gamma_{\mathrm{inv}})$, where Γ_{SM} is set to 4.07 MeV. Figure 8 (right) shows the 90% CL upper limits on the spin-independent DM-nucleon scattering cross section as a function of m_χ, for both the scalar and the fermion DM scenarios. These limits are computed at 90% CL so that they can be compared with those from direct detection experiments such as LUX [67], PandaX-II [68], CDMSlite [69] and CRESST-II [70], which provide the strongest constraints in the m_χ range probed by this search. In the context of Higgs-portal models, the result presented in this letter provides the most stringent limits for m_χ smaller than 20 or 7 GeV, assuming a fermion or a scalar DM candidate, respectively.

9 Summary

A search for invisible decays of the Higgs boson is presented using 13 TeV proton-proton collision data, collected by the CMS experiment in 2016 and corresponding to an integrated luminosity of 35.9 fb^{-1}. The search targets events in which the Higgs boson is produced through vector boson fusion (VBF). The data are found to be consistent with the predicted standard model (SM) backgrounds. An observed (expected) upper limit of 0.28 (0.21) is set, at 95% confidence level (CL), on the invisible branching fraction, $\mathcal{B}(\mathrm{H} \to \mathrm{inv})$, of the 125 GeV Higgs

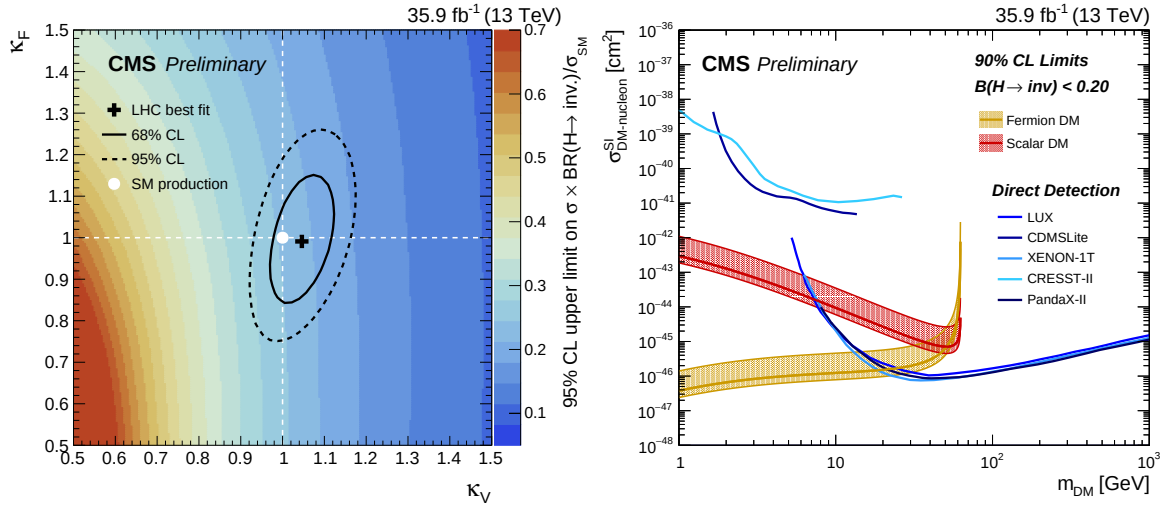

Figure 8: On the left, observed 95% CL upper limits on $\mathcal{B}(\mathrm{H} \to \mathrm{inv})$ for a Higgs boson with a mass of 125 GeV, whose production cross sections varies as a function of the coupling modifiers κ_V and κ_F. Their best estimate, along with the 68 and 95% CL contours from Ref. [4], are also reported. The SM prediction corresponds to $\kappa_V = \kappa_F = 1$. On the right, 90% CL upper limits on the spin-independent DM-nucleon scattering cross section in Higgs-portal models assuming a scalar (red solid line) or fermion (orange solid line) DM candidate. Limits are computed as a function of m_χ and are compared to those from LUX [67], Panda-X II [68], CDMSlite [69] and CRESST-II [70] experiments.

boson. Furthermore, upper limits are also set on the product of the cross section and branching fraction of a SM-like Higgs boson particle, with mass ranging between 110 and 1000 GeV.

Finally, a combination of searches for a Higgs boson decaying to invisible particles, using 35.9 fb^{-1} of data collected by the CMS detector during 2016, is presented. The combination includes searches targeting Higgs boson production in the qqH, ZH (in which a Z boson decays to $\ell^+\ell^-$), VH (in which the vector boson decays hadronically) and ggH modes. The VBF search represents, by far, the most sensitive channel involved in the combination. No significant deviations from the SM predictions are observed in any of these searches. The combination yields an observed (expected) upper limit on $\mathcal{B}(\mathrm{H} \to \mathrm{inv})$ of 0.24 (0.18) at 95% CL, assuming SM production of the Higgs boson. The observed 90% CL limit of $\mathcal{B}(\mathrm{H} \to \mathrm{inv}) < 0.2$ is interpreted in terms of Higgs-portal models of dark matter (DM) interactions. Constraints are placed on the spin-independent DM-nucleon interaction cross section. When compared to the upper bounds from direct detection experiments, this limit provides the strongest constraints on fermion (scalar) DM particles with masses smaller than about 20 (7) GeV.

References

[1] ATLAS Collaboration, "Observation of a new particle in the search for the Standard Model Higgs boson with the ATLAS detector at the LHC", *Phys. Lett. B* **716** (2012) 1, doi:10.1016/j.physletb.2012.08.020, arXiv:1207.7214.

[2] CMS Collaboration, "Observation of a new boson at a mass of 125 GeV with the CMS experiment at the LHC", *Phys. Lett. B* **716** (2012) 30, doi:10.1016/j.physletb.2012.08.021, arXiv:1207.7235.

[3] CMS Collaboration, "Observation of a new boson with mass near 125 GeV in pp collisions at $\sqrt{s} = 7$ and 8 TeV", *JHEP* **06** (2013) 081, doi:10.1007/JHEP06(2013)081, arXiv:1303.4571.

[4] ATLAS and CMS Collaborations, "Measurements of the Higgs boson production and decay rates and constraints on its couplings from a combined ATLAS and CMS analysis of the LHC pp collision data at $\sqrt{s} = 7$ and 8 TeV", *JHEP* **08** (2016) 045, doi:10.1007/JHEP08(2016)045, arXiv:1606.02266.

[5] G. Belanger et al., "The MSSM invisible Higgs in the light of dark matter and g-2", *Phys. Lett. B* **519** (2001) 93–102, doi:10.1016/S0370-2693(01)00976-5, arXiv:hep-ph/0106275.

[6] A. Datta, K. Huitu, J. Laamanen, and B. Mukhopadhyaya, "Invisible Higgs in theories of large extra dimensions", *Phys. Rev.* **D70** (2004) 075003, doi:10.1103/PhysRevD.70.075003, arXiv:hep-ph/0404056.

[7] D. Dominici and J. F. Gunion, "Invisible Higgs Decays from Higgs Graviscalar Mixing", *Phys. Rev.* **D80** (2009) 115006, doi:10.1103/PhysRevD.80.115006, arXiv:0902.1512.

[8] ATLAS Collaboration, "Constraints on new phenomena via Higgs boson couplings and invisible decays with the ATLAS detector", *JHEP* **11** (2015) 206, doi:10.1007/JHEP11(2015)206, arXiv:1509.00672.

[9] CMS Collaboration, "Searches for invisible decays of the Higgs boson in pp collisions at sqrt(s) = 7, 8, and 13 TeV", *JHEP* **02** (2017) 135, doi:10.1007/JHEP02(2017)135, arXiv:1610.09218.

[10] CMS Collaboration, "Search for invisible decays of Higgs bosons in the vector boson fusion and associated ZH production modes", *Eur. Phys. J.* **C74** (2014) 2980, doi:10.1140/epjc/s10052-014-2980-6, arXiv:1404.1344.

[11] CMS Collaboration, "Search for new physics in events with a leptonically decaying Z boson and a large transverse momentum imbalance in proton-proton collisions at $\sqrt{s}$ = 13 TeV", arXiv:1711.00431.

[12] CMS Collaboration, "Search for new physics in final states with an energetic jet or a hadronically decaying W or Z boson and transverse momentum imbalance at $\sqrt{s} = 13$ TeV", arXiv:1712.02345.

[13] R. E. Shrock and M. Suzuki, "Invisible decays of Higgs bosons", *Phy. Lett. B* **110** (1982) 250, doi:10.1016/0370-2693(82)91247-3.

[14] A. Djouadi, O. Lebedev, Y. Mambrini, and J. Quevillon, "Implications of LHC searches for Higgs–portal dark matter", *Phys. Lett.* **B709** (2012) 65–69, doi:10.1016/j.physletb.2012.01.062, arXiv:1112.3299.

[15] S. Baek, P. Ko, W.-I. Park, and E. Senaha, "Higgs Portal Vector Dark Matter : Revisited", *JHEP* **05** (2013) 036, doi:10.1007/JHEP05(2013)036, arXiv:1212.2131.

[16] A. Djouadi, A. Falkowski, Y. Mambrini, and J. Quevillon, "Direct Detection of Higgs-Portal Dark Matter at the LHC", *Eur. Phys. J.* **C73** (2013), no. 6, 2455, doi:10.1140/epjc/s10052-013-2455-1, arXiv:1205.3169.

[17] A. Beniwal et al., "Combined analysis of effective Higgs portal dark matter models", *Phys. Rev.* **D93** (2016), no. 11, 115016, doi:10.1103/PhysRevD.93.115016, arXiv:1512.06458.

[18] CMS Collaboration, "The CMS trigger system", *JINST* **12** (2017), no. 01, P01020, doi:10.1088/1748-0221/12/01/P01020, arXiv:1609.02366.

[19] CMS Collaboration, "The CMS experiment at the CERN LHC", *JINST* **3** (2008) S08004, doi:10.1088/1748-0221/3/08/S08004.

[20] CMS Collaboration, "Particle-flow reconstruction and global event description with the CMS detector", *JINST* **12** (2017), no. 10, P10003, doi:10.1088/1748-0221/12/10/P10003, arXiv:1706.04965.

[21] M. Cacciari, G. P. Salam, and G. Soyez, "The Anti-k(t) jet clustering algorithm", *JHEP* **04** (2008) 063, doi:10.1088/1126-6708/2008/04/063, arXiv:0802.1189.

[22] M. Cacciari, G. P. Salam, and G. Soyez, "FastJet User Manual", *Eur. Phys. J.* **C72** (2012) 1896, doi:10.1140/epjc/s10052-012-1896-2, arXiv:1111.6097.

[23] CMS Collaboration, "Jet energy scale and resolution in the CMS experiment in pp collisions at 8 TeV", *JINST* **12** (2017), no. 02, P02014, doi:10.1088/1748-0221/12/02/P02014, arXiv:1607.03663.

[24] CMS Collaboration, "Performance of the CMS missing transverse momentum reconstruction in pp data at $\sqrt{s}$ = 8 TeV", *JINST* **10** (2015), no. 02, P02006, doi:10.1088/1748-0221/10/02/P02006, arXiv:1411.0511.

[25] CMS Collaboration, "Performance of CMS muon reconstruction in pp collision events at $\sqrt{s} = 7$ TeV", *JINST* **7** (2012) P10002, doi:10.1088/1748-0221/7/10/P10002, arXiv:1206.4071.

[26] CMS Collaboration, "Performance of electron reconstruction and selection with the CMS detector in proton-proton collisions at $\sqrt{s} = 8$ TeV", *JINST* **10** (2015) P06005, doi:10.1088/1748-0221/10/06/P06005, arXiv:1502.02701.

[27] CMS Collaboration, "Reconstruction and identification of τ lepton decays to hadrons and ν_τ at CMS", *JINST* **11** (2016) P01019, doi:10.1088/1748-0221/11/01/P01019, arXiv:1510.07488.

[28] P. Nason, "A New method for combining NLO QCD with shower Monte Carlo algorithms", *JHEP* **11** (2004) 040, doi:10.1088/1126-6708/2004/11/040, arXiv:hep-ph/0409146.

[29] S. Frixione, P. Nason, and C. Oleari, "Matching NLO QCD computations with Parton Shower simulations: the POWHEG method", *JHEP* **11** (2007) 070, doi:10.1088/1126-6708/2007/11/070, arXiv:0709.2092.

[30] S. Alioli, P. Nason, C. Oleari, and E. Re, "A general framework for implementing NLO calculations in shower Monte Carlo programs: the POWHEG BOX", *JHEP* **06** (2010) 043, doi:10.1007/JHEP06(2010)043, arXiv:1002.2581.

[31] E. Bagnaschi, G. Degrassi, P. Slavich, and A. Vicini, "Higgs production via gluon fusion in the POWHEG approach in the SM and in the MSSM", *JHEP* **02** (2012) 088, doi:10.1007/JHEP02(2012)088, arXiv:1111.2854.

[32] P. Nason and C. Oleari, "NLO Higgs boson production via vector-boson fusion matched with shower in POWHEG", *JHEP* **02** (2010) 037, doi:10.1007/JHEP02(2010)037, arXiv:0911.5299.

[33] LHC Higgs Cross Section Working Group Collaboration, "Handbook of LHC Higgs Cross Sections: 4. Deciphering the Nature of the Higgs Sector", doi:10.23731/CYRM-2017-002, arXiv:1610.07922.

[34] C. Anastasiou et al., "High precision determination of the gluon fusion Higgs boson cross-section at the LHC", *JHEP* **05** (2016) 058, doi:10.1007/JHEP05(2016)058, arXiv:1602.00695.

[35] D. de Florian, G. Ferrera, M. Grazzini, and D. Tommasini, "Higgs boson production at the LHC: transverse momentum resummation effects in the $H \to 2\gamma$, $H \to WW \to \ell\nu\ell\nu$ and $H \to ZZ \to 4\ell$ decay modes", *JHEP* **06** (2012) 132, doi:10.1007/JHEP06(2012)132, arXiv:1203.6321.

[36] M. Grazzini and H. Sargsyan, "Heavy-quark mass effects in Higgs boson production at the LHC", *JHEP* **09** (2013) 129, doi:10.1007/JHEP09(2013)129, arXiv:1306.4581.

[37] ATLAS, CMS Collaboration, "Combined Measurement of the Higgs Boson Mass in pp Collisions at $\sqrt{s} = 7$ and 8 TeV with the ATLAS and CMS Experiments", *Phys. Rev. Lett.* **114** (2015) 191803, doi:10.1103/PhysRevLett.114.191803, arXiv:1503.07589.

[38] J. Alwall et al., "The automated computation of tree-level and next-to-leading order differential cross sections, and their matching to parton shower simulations", *JHEP* **07** (2014) 079, doi:10.1007/JHEP07(2014)079, arXiv:1405.0301.

[39] T. Sjöstrand et al., "An Introduction to PYTHIA 8.2", *Comput. Phys. Commun.* **191** (2015) 159, doi:10.1016/j.cpc.2015.01.024, arXiv:1410.3012.

[40] CMS Collaboration, "Event generator tunes obtained from underlying event and multiparton scattering measurements", *Eur. Phys. J. C* **76** (2016) 155, doi:10.1140/epjc/s10052-016-3988-x, arXiv:1512.00815.

[41] J. Alwall et al., "Comparative study of various algorithms for the merging of parton showers and matrix elements in hadronic collisions", *Eur. Phys. J.* **C53** (2008) 473–500, doi:10.1140/epjc/s10052-007-0490-5, arXiv:0706.2569.

[42] NNPDF Collaboration, "Parton distributions for the LHC Run II", *JHEP* **04** (2015) 040, doi:10.1007/JHEP04(2015)040, arXiv:1410.8849.

[43] GEANT4 Collaboration, "GEANT4: A Simulation toolkit", *Nucl. Instrum. Meth.* **A506** (2003) 250–303, doi:10.1016/S0168-9002(03)01368-8.

[44] CMS Collaboration, "Performance of missing energy reconstruction in 13 TeV pp collision data using the CMS detector", CMS Physics Analysis Summary CMS-PAS-JME-16-004, 2016.

[45] CMS Collaboration, "Performance of photon reconstruction and identification with the CMS detector in proton-proton collisions at $\sqrt{s} = 8$ TeV", *JINST* **10** (2015) P08010, doi:10.1088/1748-0221/10/08/P08010, arXiv:1502.02702.

[46] CMS Collaboration, "Identification of b-quark jets with the CMS experiment", *JINST* **8** (2013) P04013, doi:10.1088/1748-0221/8/04/P04013, arXiv:1211.4462.

[47] CMS Collaboration, "Identification of heavy-flavour jets with the CMS detector in pp collisions at 13 TeV", *Submitted to: JINST* (2017) arXiv:1712.07158.

[48] J. H. Kuhn, A. Kulesza, S. Pozzorini, and M. Schulze, "Electroweak corrections to hadronic photon production at large transverse momenta", *JHEP* **03** (2006) 059, doi:10.1088/1126-6708/2006/03/059, arXiv:hep-ph/0508253.

[49] S. Kallweit et al., "NLO electroweak automation and precise predictions for W+multijet production at the LHC", *JHEP* **04** (2015) 012, doi:10.1007/JHEP04(2015)012, arXiv:1412.5157.

[50] S. Kallweit et al., "NLO QCD+EW predictions for V+jets including off-shell vector-boson decays and multijet merging", *JHEP* **04** (2016) 021, doi:10.1007/JHEP04(2016)021, arXiv:1511.08692.

[51] K. Arnold et al., "VBFNLO: A Parton level Monte Carlo for processes with electroweak bosons", *Comput. Phys. Commun.* **180** (2009) 1661–1670, doi:10.1016/j.cpc.2009.03.006, arXiv:0811.4559.

[52] J. Baglio et al., "Release Note - VBFNLO 2.7.0", arXiv:1404.3940.

[53] J. M. Lindert et al., "Precise predictions for $V+$ jets dark matter backgrounds", *Eur. Phys. J.* **C77** (2017), no. 12, 829, doi:10.1140/epjc/s10052-017-5389-1, arXiv:1705.04664.

[54] CMS Collaboration, "Search for new physics with jets and missing transverse momentum in pp collisions at $\sqrt{s} = 7$ TeV", *JHEP* **08** (2011) 155, doi:10.1007/JHEP08(2011)155, arXiv:1106.4503.

[55] M. Czakon, D. Heymes, and A. Mitov, "High-precision differential predictions for top-quark pairs at the LHC", *Phys. Rev. Lett.* **116** (2016) 082003, doi:10.1103/PhysRevLett.116.082003, arXiv:1511.00549.

[56] CMS Collaboration, "Measurement of the ZZ production cross section and Z $\to \ell^+\ell^-\ell'^+\ell'^-$ branching fraction in pp collisions at $\sqrt{s} = 13$ TeV", *Phys. Lett. B* **763** (2016) 280, doi:10.1016/j.physletb.2016.10.054, arXiv:1607.08834.

[57] CMS Collaboration, "Measurement of the WZ production cross section in pp collisions at $\sqrt{s} = 13$ TeV", *Phys. Lett. B* **766** (2017) 268, doi:10.1016/j.physletb.2017.01.011, arXiv:1607.06943.

[58] CMS Collaboration Collaboration, "CMS Luminosity Measurements for the 2016 Data Taking Period", Technical Report CMS-PAS-LUM-17-001, CERN, Geneva, 2017.

[59] CMS Collaboration, "Simplified likelihood for the re-interpretation of public CMS results", CMS Note CMS-NOTE-2017-001, 2017.

[60] T. Junk, "Confidence level computation for combining searches with small statistics", *Nucl. Instrum. Meth. A* **434** (1999) 435, doi:10.1016/S0168-9002(99)00498-2, arXiv:hep-ex/9902006.

[61] A. L. Read, "Presentation of search results: the CL_s technique", *J. Phys. G* **28** (2002) 2693, doi:10.1088/0954-3899/28/10/313.

[62] G. Cowan, K. Cranmer, E. Gross, and O. Vitells, "Asymptotic formulae for likelihood-based tests of new physics", *Eur. Phys. J. C* **71** (2011) 1554, doi:10.1140/epjc/s10052-011-1554-0, arXiv:1007.1727. [Erratum: doi:10.1140/epjc/s10052-013-2501-z].

[63] The ATLAS Collaboration, The CMS Collaboration, The LHC Higgs Combination Group Collaboration, "Procedure for the LHC Higgs boson search combination in Summer 2011", Technical Report CMS-NOTE-2011-005. ATL-PHYS-PUB-2011-11, CERN, Geneva, Aug, 2011.

[64] CMS Collaboration, "Search for a Higgs boson in the mass range from 145 to 1000 GeV decaying to a pair of W or Z bosons", *JHEP* **10** (2015) 144, doi:10.1007/JHEP10(2015)144, arXiv:1504.00936.

[65] LHC Higgs Cross Section Working Group Collaboration, "Handbook of LHC Higgs Cross Sections: 3. Higgs Properties", doi:10.5170/CERN-2013-004, arXiv:1307.1347.

[66] R. D. Young and A. W. Thomas, "Octet baryon masses and sigma terms from an SU(3) chiral extrapolation", *Phys. Rev.* **D81** (2010) 014503, doi:10.1103/PhysRevD.81.014503, arXiv:0901.3310.

[67] LUX Collaboration, "Results from a search for dark matter in the complete LUX exposure", *Phys. Rev. Lett.* **118** (2017), no. 2, 021303, doi:10.1103/PhysRevLett.118.021303, arXiv:1608.07648.

[68] PandaX-II Collaboration, "Dark Matter Results from First 98.7 Days of Data from the PandaX-II Experiment", *Phys. Rev. Lett.* **117** (2016), no. 12, 121303, doi:10.1103/PhysRevLett.117.121303, arXiv:1607.07400.

[69] SuperCDMS Collaboration, "New Results from the Search for Low-Mass Weakly Interacting Massive Particles with the CDMS Low Ionization Threshold Experiment", *Phys. Rev. Lett.* **116** (2016), no. 7, 071301, doi:10.1103/PhysRevLett.116.071301, arXiv:1509.02448.

[70] CRESST Collaboration, "Results on light dark matter particles with a low-threshold CRESST-II detector", *Eur. Phys. J.* **C76** (2016), no. 1, 25, doi:10.1140/epjc/s10052-016-3877-3, arXiv:1509.01515.

A Supplementary material

The two observables which show the largest discrimination power between qqH signal events and V+jets backgrounds, arising either from QCD or EW production, are the invariant mass of the VBF jet pair and their pseudorapidity separation. Figure 9 shows a comparison between the shapes of the m_{jj} (left) and the $\Delta\eta_{jj}$ (right) distributions of simulated signal and V+jets background events, where Z + jets and W + jets processes are summed together.

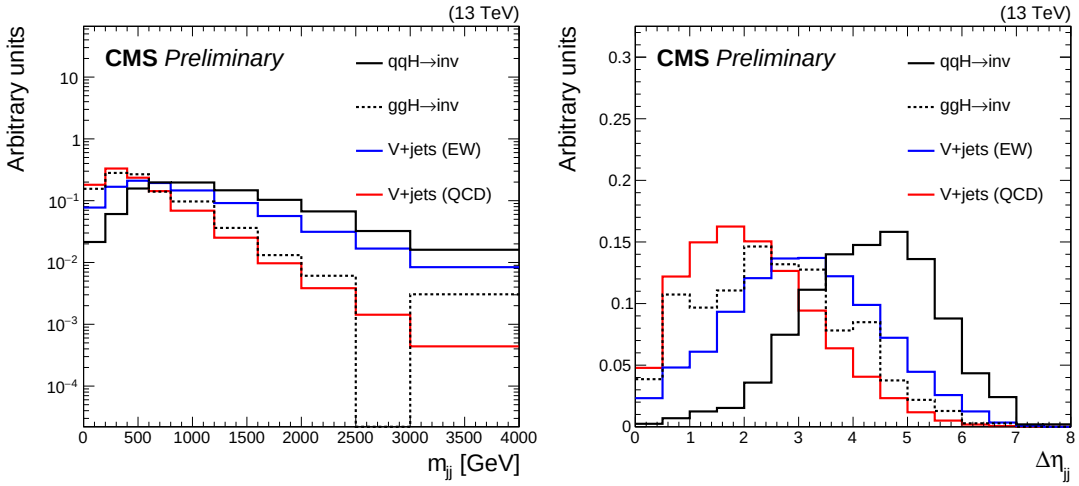

Figure 9: Comparison between the shapes of the m_{jj} (left) and the $\Delta\eta_{jj}$ (right) distributions of Higgs invisible signal events, produced by qqH (solid black) and ggH (dashed black) mechanisms, and V+jets backgrounds from both QCD (red) and EW (blue) production.

To assess the level of agreement between data and MC obtained through the application of p_T-m_{jj} dependent NLO corrections to both the V+jets (QCD) and V+jets (EW) processes, the ratio between the number of Z + jets and W + jets events in the control samples is used as figure of merit. Figure 10 shows the Z + jets/W + jets ratio for the muon (left) and electron (right) final states as measured in the control regions as a function of m_{jj}. Good agreement is observed between data and simulation after applying the NLO corrections described in Section 6.2, and local differences are covered by the systematic uncertainties applied on the ratio.

The correlations between the predicted background yields across the m_{jj} bins in the shape analysis signal region are reported in Figure 11, obtained from a combined fit in all the control samples excluding the data in the signal region. This result, along with the background yields listed in Table 3, can be used with the simplified likelihood approach detailed in Ref. [59] to reinterpret the analysis results in different models to those presented in this letter.

Figure 12 (left) shows the m_{jj} distribution in the dimuon control region, obtained after applying the cut-and-count selection, where backgrounds are normalized either to the post-fit rate obtained from the control-region-only fit (dashed red line) or to the prediction from a background-only fit performed across signal and control regions (solid blue line) while, on the right, the $\Delta\eta_{jj}$ spectrum is reported. Similarly, Fig. 13, Fig. 14 and Fig.15 show the same distributions and fit results for the dielecton, single-muon and single-electron control samples, respectively.

Figure 16 shows the cut-and-count analysis upper limits on $\sigma\mathcal{B}(H \to \text{inv})/\sigma_{SM}$ for the SM-like Higgs boson scenario as a function of m_H. Since a single-bin fit cannot distinguish between mass hypotheses, no mass dependent trends of the observed limit are observed compared to the median expectation.

Table 7 lists the correlations applied to the main sources of systematic uncertainties across the

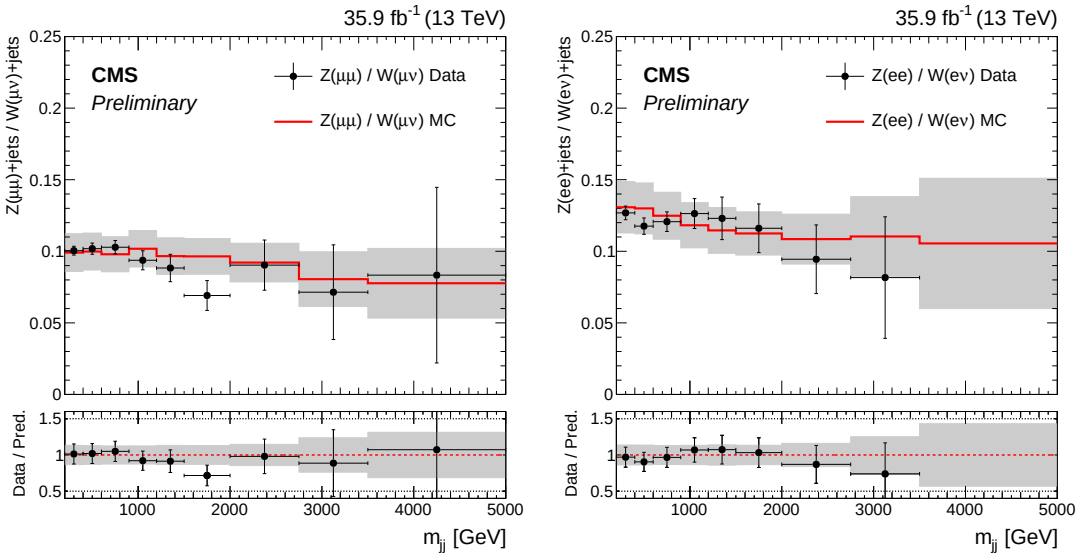

Figure 10: Comparison between data and simulation of the $Z(\mu\mu)$+jets/$W(\mu\nu)$+jets (left) and $Z(ee)$+jets/$W(e\nu)$+jets (right) ratios, as a function of m_{jj}, computed in the shape analysis phase space. In the lower panels, ratios of data with the pre-fit background prediction are reported. The gray bands include both the pre-fit theoretical and experimental uncertainties, as well as the statistical uncertainty in the simulation.

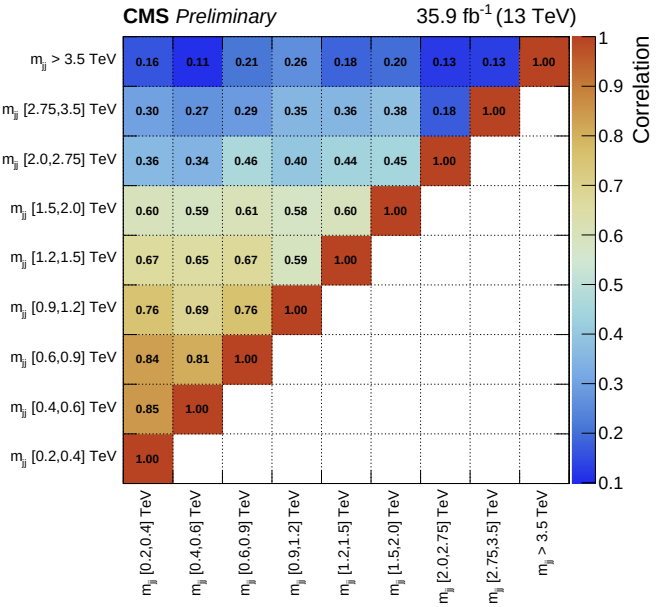

Figure 11: Correlation between the predicted background yields across the m_{jj} bins of the shape analysis signal region. The boundaries of the m_{jj} bins, expressed in TeV, are shown at the bottom and on the left.

searches involved in the combination.

Finally, Fig. 17 shows a three-dimensional display of one event characterized by large p_T^{miss} and two jets in the final state with high m_{jj}, which passes the signal region selection. In addition, Fig. 18 reports one high m_{jj} event selected in the dimuon control sample.

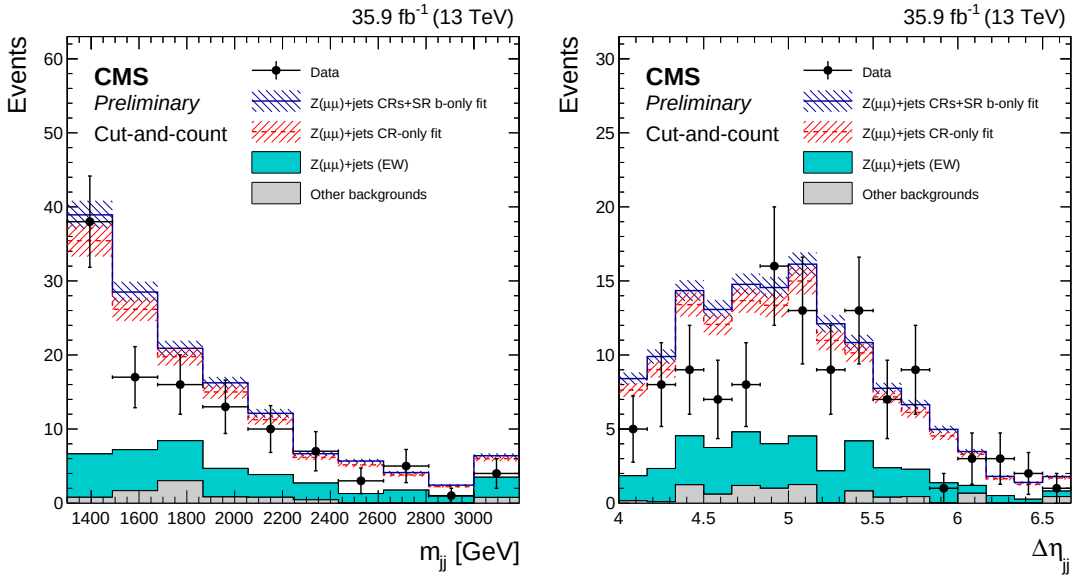

Figure 12: The observed m_{jj} (left) and $\Delta\eta_{jj}$ (right) distributions in the dimuon control sample of the cut-and-count analysis compared to the post-fit backgrounds from various SM processes. The predicted background normalizations are obtained either from a combined fit to the data in all the control samples but excluding the signal region (dashed red line) or from a background-only fit performed across signal and control regions (blue solid line).

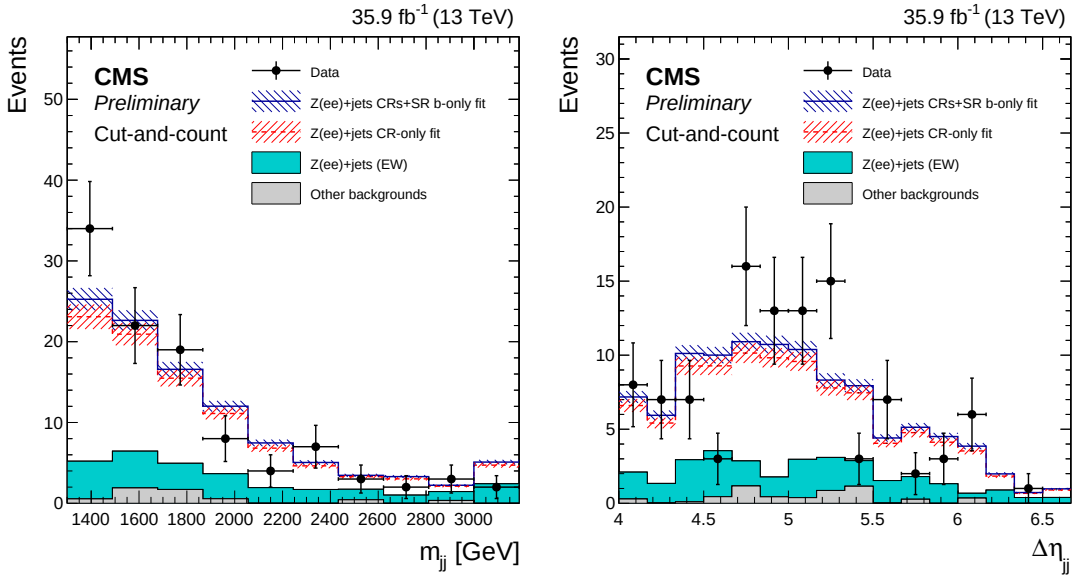

Figure 13: The observed m_{jj} (left) and $\Delta\eta_{jj}$ (right) distributions in the dielectron control sample of the cut-and-count analysis compared to the post-fit backgrounds from various SM processes. The predicted background normalizations are obtained either from a combined fit to the data in all the control samples but excluding the signal region (dashed red line) or from a background-only fit performed across signal and control regions (blue solid line).

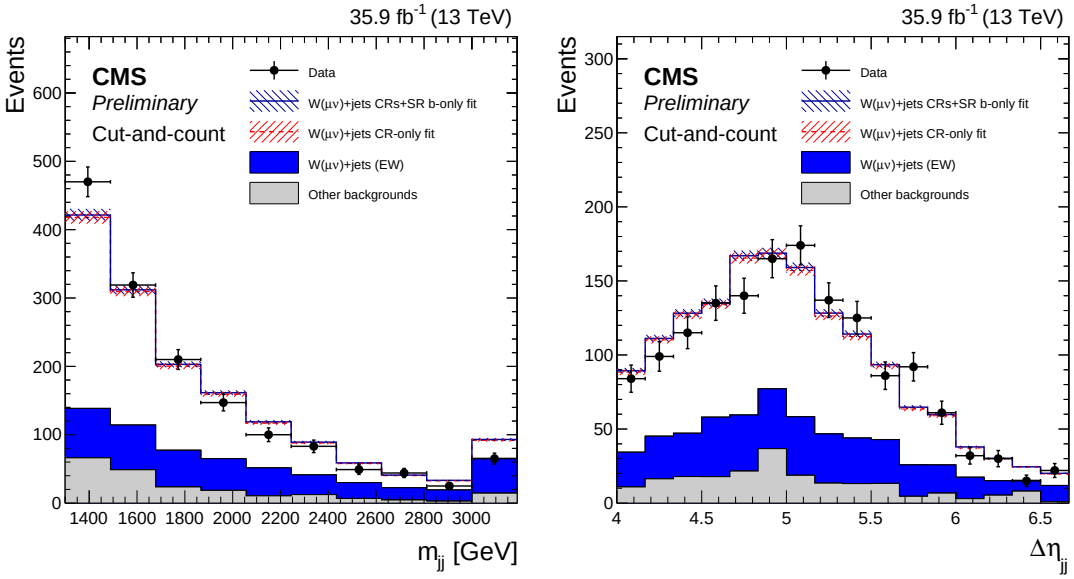

Figure 14: The observed m_{jj} (left) and $\Delta\eta_{jj}$ (right) distributions in the single-muon control sample of the cut-and-count analysis compared to the post-fit backgrounds from various SM processes. The predicted background normalizations are obtained either from a combined fit to the data in all the control samples but excluding the signal region (dashed red line) or from a background-only fit performed across signal and control regions (blue solid line).

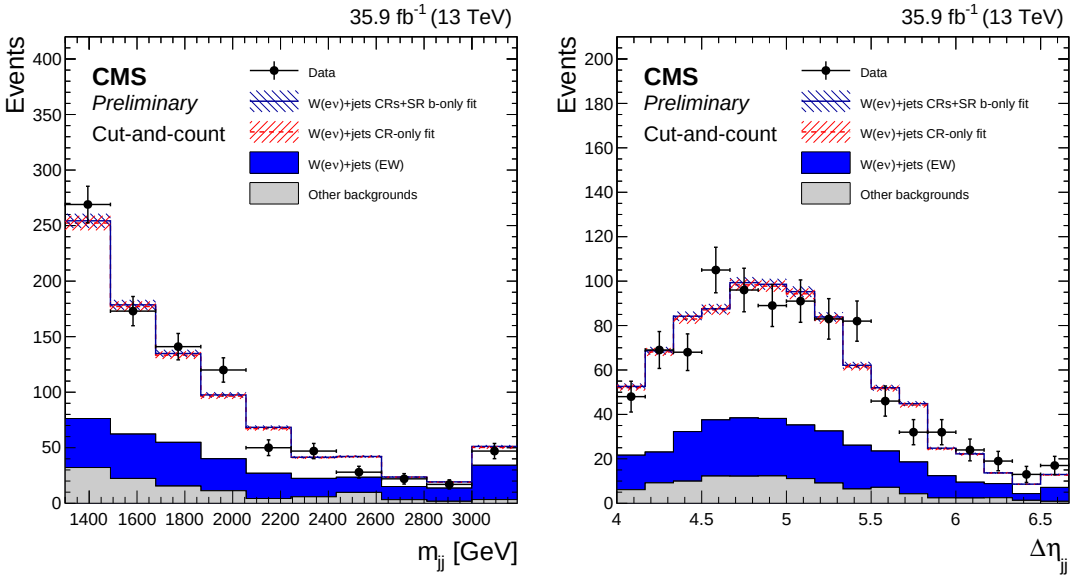

Figure 15: The observed m_{jj} (left) and $\Delta\eta_{jj}$ (right) distributions in the single-electron control sample of the cut-and-count analysis compared to the post-fit backgrounds from various SM processes. The predicted background normalizations are obtained either from a combined fit to the data in all the control samples but excluding the signal region (dashed red line) or from a background-only fit performed across signal and control regions (blue solid line).

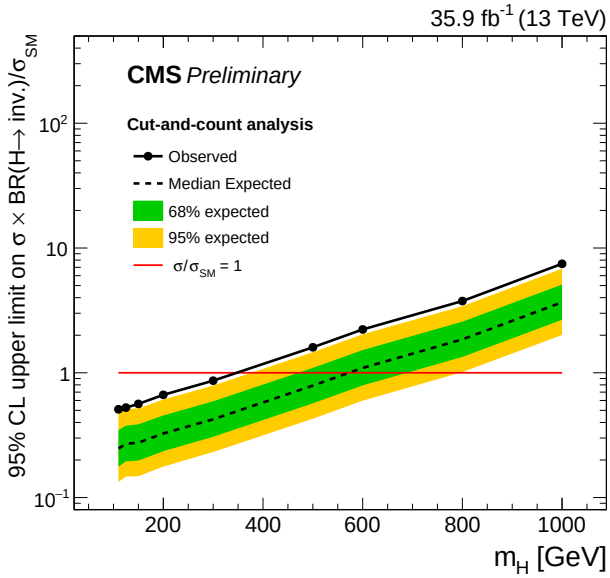

Figure 16: Expected (dashed line) and observed (solid line) 95% CL upper limits on $\sigma\mathcal{B}(\mathrm{H} \to \mathrm{inv})/\sigma_{\mathrm{SM}}$ for a SM-like Higgs boson particle as a function of its mass (m_{H}) obtained from the cut-and-count analysis. The 68 and 95% CL intervals around the expected upper limit are also reported.

Table 7: Correlations applied to the main sources of systematic uncertainties that affect the searches for invisible decays of the Higgs boson involved in the combination.

Source of uncertainty	Correlation
Experimental uncertainties	
Luminosity	Correlated across searches
Muon id. eff.	Correlated across searches
Muon reco. eff.	Correlated across searches
Electron id. eff.	Correlated across searches
Electron reco. eff.	Correlated across searches
Muon veto eff.	Correlated across searches
Electron veto eff.	Correlated across searches
B-jet veto eff.	Correlated across searches
Hadronic τ veto eff.	Correlated across searches
Muon energy scale	Correlated across searches
Electron energy scale	Correlated across searches
Jet energy scale	Correlated across ggH, $V(qq')$H and $Z(\ell\ell)$H searches
$p_{\mathrm{T}}^{\mathrm{miss}}$ energy scale	Correlated across ggH, $V(qq')$H and $Z(\ell\ell)$H searches
Muon mis-tag rate	Correlated across single-lepton CR of ggH, $V(qq')$H and qqH searches
Electron mis-tag rate	Correlated across single-lepton CR of ggH, $V(qq')$H and qqH searches
$p_{\mathrm{T}}^{\mathrm{miss}}$ trigger eff.	Correlated across ggH, $V(qq')$H and qqH searches
Electron trigger eff.	Correlated across ggH, $V(qq')$H and qqH searches
Theoretical uncertainties on SM backgrounds	
VV inclusive cross sec.	Correlated across ggH, $V(qq')$H and qqH searches
Top-quark inclusive cross sec.	Correlated across ggH, $V(qq')$H and qqH searches
VV acceptance	Correlated across ggH, $V(qq')$H and qqH searches
Top-quark acceptance	Correlated across ggH, $V(qq')$H and qqH searches
$\mathrm{Z}+\mathrm{jets}/\mathrm{W}+\mathrm{jets}$ ratio vs $p_{\mathrm{T}}^{\mathrm{miss}}$	Correlated between ggH and $V(qq')$H searches
$\mathrm{Z}+\mathrm{jets}/\gamma$+jets ratio vs $p_{\mathrm{T}}^{\mathrm{miss}}$	Correlated between ggH and $V(qq')$H searches
Theoretical uncertainties on Higgs production	
ggH, qqH and VH inclusive cross sec. from QCD-scale	Correlated across searches
ggH, qqH and VH inclusive cross sec. from PDF	Correlated across searches
ggH, qqH and VH acceptance from QCD-scale	Correlated across searches
ggH, qqH and VH acceptance from PDF	Correlated across searches
ggH Higgs p_{T}-dependent unc.	Correlated between ggH and $V(qq')$H searches
VH EWK corrections	Correlated between $V(qq')$H and $Z(\ell\ell)$H searches

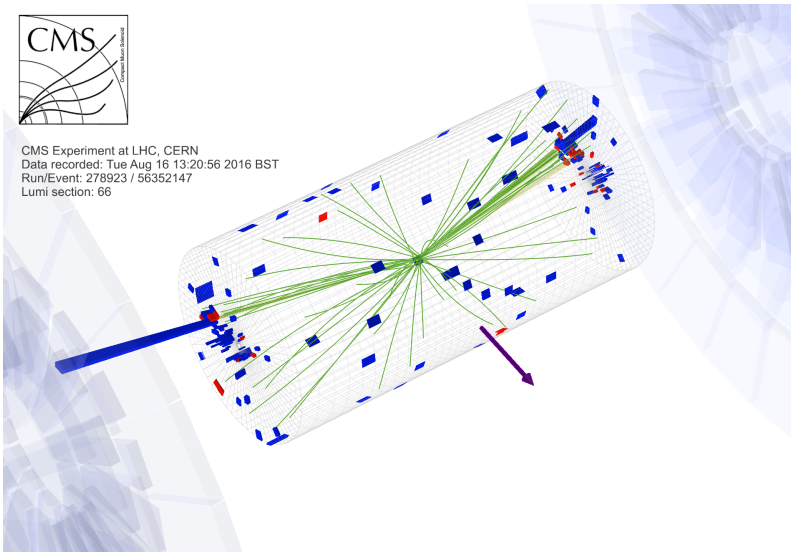

Figure 17: Event display showing the three-dimensional view of one event passing the signal region selection with the following properties: $p_{\mathrm{T}}^{\mathrm{miss}}$ of 355 GeV, leading (trailing) jet p_{T} of 177 (107) GeV, $m_{\mathrm{jj}} = 1380$ GeV, $\Delta\eta_{\mathrm{jj}} = 4.6$ and $\Delta\phi_{\mathrm{jj}}$ of 0.02 radians.

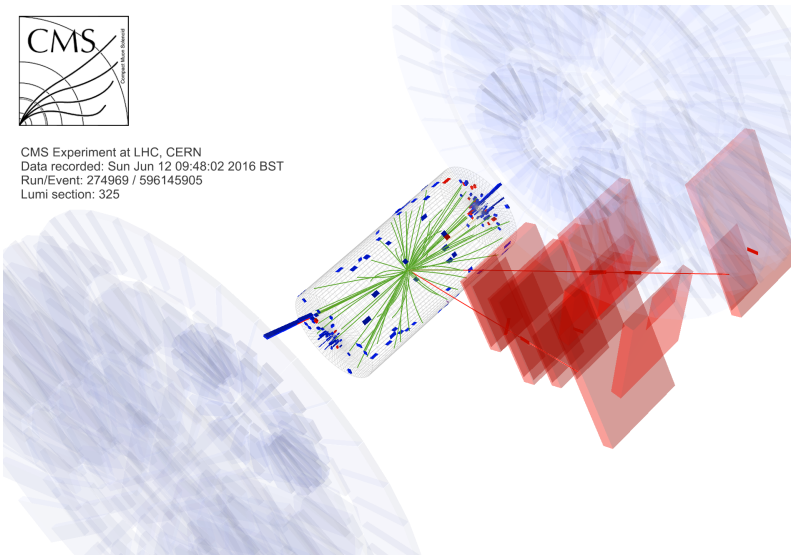

Figure 18: Event display showing the three-dimensional view of an event passing the dimuon control sample selection with the following properties: hadronic recoil p_{T} of 276 GeV, leading (trailing) jet p_{T} of 194 (141) GeV, leading (trailing) muon p_{T} of 132 (126) GeV, $m_{\mathrm{jj}} = 1393$ GeV, $\Delta\eta_{\mathrm{jj}} = 4.3$ and $\Delta\phi_{\mathrm{jj}}$ of 1.26 radians.